NTNU

Norwegian University of
Science and Technology

Cancellation of Movement Artifacts in GlucoseSensor Data

Roar Tordahl Nøstbakken

Master of Science in Industrial Cybernetics
Submission date: June 2017
Supervisor: Øyvind Stavdahl, ITK
Co-supervisor: Odd Martin Staal, Prediktor Medical AS

Norwegian University of Science and Technology
Department of Engineering Cybernetics

NTNU
Norwegian University of
Science and Technology

Faculty of Information technology,
Mathematics and Electrical Engineering
Department of Engineering Cybernetics

Master's Thesis

Student's name: Roar Tordahl Nøstbakken

Field: Engineering Cybernetics

Title (Norwegian): Kansellering av bevegelsesindusert støy i data fra GlukoseSensor

Title (English): Cancellation of Movement Artifacts in GlucoseSensor Data

Description:
A project work has been done in autumn 2016, investigating measurement of signals related to movement artifacts in the BioMKR sensor. This work considered different approaches for measuring pressure of the device against the skin, and focused on Force Sensitive Resistors (FSRs). Further work is needed to improve the pressure measurement and find a mechanical design that enables a pressure sensor to be included in the BioMKR.

1. Investigate through literature study methods for removing motion induced artifacts in wearable devices
2. Investigate other methods to do force/pressure measurement with focus on repeatability, and compare against the FSR method. Select the method that gives the best compromise between quality of measurement and implementability in a small battery-powered wearable device.
3. Implement the chosen solution and integrate it with the BioMKR in a fully integrated and assembled device that can be used for stand-alone logging of data
4. Record pressure data along with BioMKR data and investigate the influence of pressure on the measurements
5. Suggest algorithms for compensating pressure/external force artefacts in the BioMKR signals based on the recorded signals

Advisor(s): Øyvind Stavdahl, Assoc. Professor, Dept. of Engineering Cybernetics, NTNU
Odd Martin Staal, Prediktor Medical AS

Trondheim, 12.12.2016

Øyvind Stavdahl
Supervisor

Preface

This thesis is submitted in fulfillment of my 2 year Master of Science at the Norwegian University of Science and Technology (NTNU), Department of Engineering Cybernetics.

The work presented here has been carried out through the spring of 2017, and is regarded as the primary source of my findings. This work is my contribution in the progress of improving the BioMKR device, which I hope to see on the market in the near future.

There are many people that have helped me throughout this period, who have helped me, motivated me and made this whole process possible.

I would like to thank Odd Martin Staal with Prediktor for excellent cooperation and guidance throughout this semester. His knowledge and experience have taught me many things, as well providing me with valuable feedback to my work. A thank you to Zaid Hamed with Prediktor is also appropriate, for helping me with the hardware implementation and troubleshooting.

A special thank you to all the employees working in the Engineering Workshop at the Department of Engineering Cybernetics, for helping me construct the necessary testing tools used in this thesis.

Thank you to everyone that has helped me reach my milestone in acquiring a Master of Science degree. Through years of motivation, constructive feedback and great support, I would like to give a huge thanks to my parents. You have done everything to help me achieve this, and I am forever grateful.

Last, but not least, a huge thank you to my loving girlfriend and mother of my child, Henriette Andrea, for taking excellent care of our son Oscar, enabling me to focus on my work.

Trondheim, June 2017

Roar Tordahl Nøstbakken

Abstract

The BioMKR wearable device developed by Prediktor Medical is aiming to be the first non-invasive continuous glucose monitoring device on the consumer market. The data gathered by the device, however, contains movement artifacts that limit its performance. The artifacts responsible for this deviation is believed to be correlated with the external forces acting on the device. Therefore, the use of a force sensor as an auxiliary measurement is evaluated. A Force Sensing Resistor is integrated with the BioMKR circuitry to enable stand-alone logging of data. The main purpose for this study is to evaluate the possibility of using the force measurements to characterize the signal perturbations, and use the data set to compensate for faulty readings.

This thesis evaluates the influence the external forces captured by the FSR sensor has on the recorded near infrared signals. Two prototypes have been tested, where the second prototype needed additional improvement of the FSR actuating system. Different adapters for the actuating system was developed, and their performance are measured with respect to FSR signal stability, sensitivity and skin irritation. Test conducted with the prototypes replicate real use of the device, and consists of strap test, night test, temperature test and external force test.

The results from night testing have been modeled using PLSR, which showed some predictive properties. Building a model from one session and using it to predict the FSR from another session proved unsuccessful, implying weak correlation between the FSR signal and NIR signal. The alteration of the optical properties of the tissue as a reponse to applied pressure is believed to affect the NIR signals in a way that the FSR alone is not able to model.

Using the force signal as an event marker for NIR changes, however, proved to be very good. It can be shown that the FSR successfully captures every significant NIR change as a result from involuntary movement during sleep.

It is advised that the force signal should be used together with accelerometer and other BioMKR parameters in determine the level of trust the resulting NIR signal has in estimating the correct blood glucose. Further evaluation on filtering methods to compensate for erroneous BioMKR data is also advised.

Sammendrag

Prediktor Medical har utviklet en kroppsbåren glukoseenhet som har mulighet til å måle blodsukker kontinuerlig ved hjelp av ikke-invasive metoder, og sikter til å være den første av sitt slag. Målinger gjort med enheten er imidlertid påvirket av bevegelsesindusert støy som begrenser påliteligheten til de estimerte verdier. Eksterne krefter/trykk som påføres enheten mistenkes å være en mulig kilde til avvikene sett i BioMKR data. Ved å implementere en Force Sensing Resistor (FSR) i enheten kan man utføre eksperimenter hvor ytre krefter måles samtidig som BioMKR opptak.

Hovedmålet med denne studien er å undersøke muligheten til å bruke målinger gjort med kraftsensorer til å karakterisere avvik som oppstår i BioMKR data, og etterhvert bruke disse målingene til å korrigere feil gjort av enheten.

Arbeidet dokumentert i denne rapporten undersøker innflytelsen av de dataen samlet av FSR har på nær-infrarøde signaler (NIR) som sendes og plukkes opp av glukosemåleren. To forskjellige prototyper er blitt testet, hvor forskjellene lå i mekanisk design. Forskjellige adaptere til Prototype II er blitt evaluert i forhold til stabilitet og komfort. Testene som er utført skal etterligne situasjoner som kan oppstå under daglig bruk av enheten, og omfatter tester med forskjellig båndstramming, data samlet under nattopptak, temperatur respons og repons på eksterne krefter.

Resultat fra nattopptak har blitt modellert ved bruk av Partial Least Squares Regression (PLSR). Dette gav noen prediktive evner, men var begrenset til hver enkelt test. Å bruke en PLSR modell fra et nattopptak til å prediktere FSR signalet i et annet viste seg å være mislykket. Dette indikerer dårlig korrelasjon mellom NIR signalene og kraftsignalene tatt opp av FSR. Vevsforandringer som et resultat av ytre krefter er mistenkt i å ha en effekt på NIR signalene som en kraftsensor alene ikke greier å modelere.

Data samlet av kraftsensoren kan derimot brukes som en hendelsesmarkør. FSR-en lykkes i å registrere alle betydelige endringer i NIR data fra nattopptak. Før forskjellige filtermetoder er undersøkt og testet med data fra FSR, er det anbefalt å bruke den sammen med akselerometeret til å overvåke mer eller mindre signifikante endringer i NIR data, for å avgjøre troverdigheten til estimert glukose.

Table of Contents

Aim of the study

The aim of this study is to evaluate the possibility of using force/pressure data gathered by sensors inside the BioMKR device as a method for motion artifact detection and reduction. It is believed that the forces contribute in perturbing the BioMKR data, by moving the device out of place. The tests conducted are done to replicate real use of the device. The end goal is to cancel out the noise components in the measured BioMKR data, and produce correct and reliable glucose estimates for the subject under evaluation.

Authors contributions

Every test procedure has been drawn by the author, as well the designing of auxiliary test equipment such as the NIR test block and adapters.

Sensor evaluation, configuration, construction, as well as measurement circuit for initial testing has been done by the author. The feedback to Prediktor from authors experience in regards to FSR circuitry lead to the choice of certain components.

The software described in Section 2.1.2 was written by the author, and the source code will be submitted as a separate .zip-file.

The contents presented in Section 1.4 is based on the work of others, and is the authors interpretation of the literature read.

Structure of the thesis

The outline of the report has the following chapters:

Introduction covers a broad view of the problem description, with introduction to the problem, literature review of the work of others, as well as alternative suggestions to the approached solution. Point 1 from the problem description will be addressed in Section 1.4.3, while point 2 will be discussed in Section 1.5.

Materials and Methods gives an overview of the equipment used in this work, as well as presenting the tests conducted. The implementation of the sensor (Point 3 from problem description) will be described in Sections 2.1.5 and 2.1.6.

Results presents the results from the tests described in the previous chapter.

Discussion will evaluate the influence of pressure on the measurements gathered from the test results (Point 4 in problem description). Point 5 in problem description is addressed in the end of this chapter, where a method for how to use the recorded sensor signals towards motion artifact cancellation is drawn out in Section 4.6.

Conclusion presents the conclusions and suggestions for future work

Chapter 1

Introduction

1.1 Wearable technology

Wearable technology, wearable devices, or simply wearables are electronic devices worn on the body of the user, and with the help of microcontrollers and various sensors are able to gather/give information to its user about physiological, geographical and/or environmental data. They are designed to help, track and make information easily accessible to the wearer in different situations, whether it is heart rate monitoring during exercise, GPS tracking in navigation or entertainment through virtual reality (VR)(Wikipedia, 2017f; Kiana and Michael, 2014).

Many products are used in fitness and health tracking, counting how many steps the wearer has taken, how many calories burnt, heart rate and distance traveled(Wiechert et al., 2016). To be able to record these factors, the device must consist of a number of sensors and integrated circuits (ICs). For example, an accelerometer can be used as a sensor in a system that keeps track of activity, electrodes interfaced with the skin can be used to measure heart rate with the right signal processing, and a GPS receiver can log distance traveled as well as current position/route. More advanced devices will include this together with communication protocols and software, enabling the device to function as a phone (i.e. Apple Watch and Samsung Gear(Wikipedia, 2017b,d))

Wearable devices include, but are not limited to, wristbands, watches, smart fabric, hearing aids and other health monitoring equipment.

1.2 Diabetes

This section is cited from (Nøstbakken, 2016).

Diabetes (*diabetes mellitus*) is a chronic, metabolic disorder where the blood glucose (blood sugar) differs from the normal range of $5-7.8$ mmol/l (Yadav et al., 2014). The disorder is divided into two main groups: Type 1 and Type 2.

People with Type 1 diabetes have had an autoimmune destruction of the insulin-producing β-cells in the *pancreas* (Bluestone et al., 2010). This is often triggered at young age, which sometimes is linked to viral infections (van der Werf et al., 2007). Living with the condition require daily insulin shots.

A combination of lifestyle and genetic factors are often the cause when people develop diabetes type 2. Decreased sensitivity to insulin (insulin resistance), decreased insulin production or a combination of the two is the physiology behind it. When the pancreas is not able to produce enough insulin to compensate for the insulin resistance, blood sugar levels increase. Obesity, little physical activity and bad eating behaviours are linked to diabetes type 2.

The insulin the pancreas produces is a hormone which increase the cells' uptake of blood glucose, and is necessary for the body to function properly.

With diabetes as a condition of growing concern with the increasing population, methods for maintaining blood glucose concentration and regulating this is important. Today's available products consists of two main invasive methods: Self Monitoring of Blood Glucose (SMBG, (Diabetes Australia.com) and Continuous Glucose Monitoring (CGM, DiabetesNet.com).

1.3 BioMKR

This section is cited from (Nøstbakken, 2016) with a few modifications.

Prediktor Medical AS, based in Fredrikstad, Norway, has developed a non-invasive continuous glucose monitoring device which aims to be the first of its kind available on the consumer market. It is aimed towards the diabetic community in making their daily monitoring and control of glucose level more convenient, less painful and provide more information in real-time than commercially available products as of today. It uses near-infrared radiation, as well as a bio impedance circuit to estimate the levels of glucose in the subjects blood.

The device has been shown to give results that are well correlated with glucose in still measurement condition (sitting still or lying in bed). However, when the movements of a free-living situation are introduced, the performance deteriorates. A major difficulty with BioMKRs performance is noise from movement artifacts. Movement artifacts are unexpected variations in the measured data, uncorrelated to the dynamics of the intended measurement. It is often a result of external force on the measuring device, which can move it out of position or press it harder against the tissue. This causes errors in the readings, and needs to be compensated for or completely canceled out. Temperature is also known to have an effect on the measurements, as well as blood flow, volumetric concentration of water in the measuring site and the optical properties of the tissue under evaluation. As force can be a source for movement artifacts, as well as force/pressure is documented to have an affect on the optical properties of the tissue (Chen et al., 2005; Chan et al., 1996; Bashkatov et al., 2005; Cugmas et al., 2014), the work presented here will focus on the forces which can be recorded with an extra sensor inside the BioMKR.

1.4 Theory

1.4.1 Basic concepts

Correct terminology and unambiguous wording are important when discussing scientific methods and results to ensure that the reader understands the content. There are a number of expressions that is important in the field of instrumentation, such as *transmitter*, *hysteresis*, *lower range value*, *span* etc.

Measurand	Physical quantity to be measured
Transmitter	An instrument converting the measurand to a interpretable signal
Lower range limit	The lowest value of the measurand that the transmitter can measure
Upper range limit	The highest value of the measurand the transmitter can measure
Range	The interval between lower and upper range limit.
Span	Difference between upper and lower range limit.
Hysteresis	The measured signal outputs different values when the measurand reaches the same point in an increasing and decreasing manner.
Symmetric Bidirectional	Zero-point lies between upper and lower range value, i.e. $\pm$5V.
Resolution	Smallest recordable change. For discrete signals, this is given by the least significant bit (LSB)

(Information from (Olsen, 2015))

1.4.2 Diffuse reflectance spectroscopy

A widely used method for optical, non-invasive measurement of biological properties is diffuse reflectance spectroscopy (DRS). The technique enables researchers and physicians to gain valuable information about the tissue and its structural and biochemical condition. The radiation from a light source (e.g. near infrared light) can, according to Reistad et al. (2015), be subjected to either specular reflection or refraction. Specular reflection is the reflection of light waves from a smooth surface, and is a phenomenon which often is tried to be avoided through optic design. Assuring good contact between the measuring probes and the sampled tissue can also help reduce specular reflection, but this is known to change the optical properties of the tissue (Chen et al., 2005). Refraction is the change in direction of wave propagation due to a change in its transmission medium(Wikipedia, 2017e,c) (e.g. glass to tissue), and the wave propagation is subjected to absorption and scattering of the light.

Optical properties of soft tissue

According to (Chan et al., 1996), the tissue can be classified as a turbid medium, and its optical properties are then characterized as the refractive index (n), anisotropic factor (g), absorption (μ_a) and scattering (μ_s) coefficients. Scattering is the dominant factor in terms of light propagation due to inhomogeneities in cellular structures and particle sizes(Chen et al., 2005). As stated in (Bashkatov et al., 2005), the optical properties of the skin layers varies due to the inhomogeneous distribution of blood vessels, chromophores and pigments in the skin.

When the tissue is under compression from the measuring probes, the biological structure in the immediate area around the contact probe changes, an thus the optical properties may change. Several studies have been conducted to investigate how DRS is influenced by the contact pressure, where (Reistad et al., 2015; Chen et al., 2005; Chan et al., 1996) reports a decrease in diffuse reflectance with increasing contact pressure for different wavelengths ([400-1600nm], [1100-1700nm], [400-850nm], respectively). Although, as presented in (Cugmas et al., 2014), several studies show inconsistencies in reported changes in transmittance, reflectance, absorption and scattering coefficients.

NIR spectroscopy and blood glucose

Near-infrared (NIR) is defined as light of wavelength between 750nm and 2500nm in the electromagnetic spectrum. It is one of the most explored technique in optical analysis of non-invasive measurement(do Amaral and Wolf, 2008), and the light emitted from the optical source penetrates the tissue depending on the wavelength. Figure 1.1 shows an example of where NIR light penetrates the *epidermis* through to *dermis*, and is reflected back to an optical photodetector. The amount of blood glucose affect the NIR by refraction, which is a result of absorbing and scattering of the light(Reistad et al., 2015). According to (Yadav et al., 2014; Chen et al., 2005), the attenuated light can be described using light transport theory:

$$I = I_0 e^{-\mu_{eff} L} \tag{1.1a}$$

$$\mu_{eff} = \sqrt{[3 \cdot \mu_a(\mu_a + \mu_s[1-g])]} \tag{1.1b}$$

where I is the reflected light intensity, I_0 is the incident light intensity, L is the length of the path of light through the tissue, and μ_a and μ_s is the coefficient of absorption and scattering, respectively. g is the anisotropic factor, which represent the average cosine of the scattering angles for photon travel path(Bashkatov et al., 2005). Both μ_a and μ_s is affected by the variation of glucose concentration (see (Yadav et al., 2014) for more details).

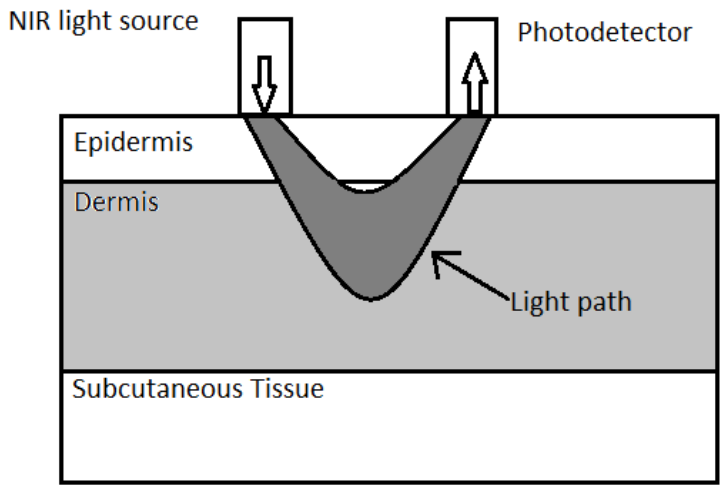

Figure 1.1: Light path and cross section of the skin

1.4.3 Methods for movement artifact removal

A well-known source of noise in signal conditioning where sensors/electrodes are fitted to the human body, are movement/motion artifacts. Movement artifacts often originate at the sensor/electrode-skin interface, and may be caused by external forces acting on the measuring component, causing it to move relative to the skin, or muscle movement in the structure beneath the component (De Luca et al., 2010). These artifacts may cause unexpected increase or decrease in the data set, unrelated to the dynamics of the measurand.

Blood flow changes are also considered a source of artifacts in NIR signals (Izzetoglu et al., 2005), and alterations of the underlying tissue in the measuring area may cause a reduced blood flow, and thereby affecting the acquired diffuse reflectance (Cugmas et al., 2014).

Reducing the motion artifacts is important in order to get a trustworthy set of data, and essential to be able to give correct information in the treatment process for any medical application. For controlled experiments and medical checkups, this may be achieved by ensuring zero movement of the subject and the measured area. But this may also be difficult to achieve, as motion artifacts are a common occurrence in Magnetic resonance imaging (MRI) evaluations, where the patient is asked to lay completely still. If the subject fails to lay still due to pain, discomfort, anxiety, or simply by the movement of the chest during MRI of the lungs, the end result can contain signal artifacts (Meier-Schroers et al., 2016).

For a wearable device developed to be worn throughout the day/night (such as the BioMKR), the limitations in movement as described above are contradicting to the purpose of this device. The artifacts need to be monitored and compensated for. Motion artifact reduction is a widely explored field of study, where multiple algorithms and numerical approximations have been tested.

Choi et al. (2007) suggests an adaptive digital filter method for movement artifact cancellation in blood pressure signals with the use of a capacitive sensor for artifact detection. A liquid filled cylinder attached to the arm serves as a load capacitor, and movement of the arm relates to the movement of the liquid inside the load capacitor. Their findings show that the timing when the capacitance change coincides well with the timings of blood pressure changes. Update the filters' coefficients depended on the timing of when capacitance changed very rapidly, and was reported to be successful in restoring the noise contaminated blood pressure signal.

Pengjun et al. (2011) investigated how the mechanical interaction between the skin and electrode influences movement artifacts in electrocardiography (ECG) recordings during various body movements. Electrode contact pressure and electrode-skin relative movement was measured, and analyzed compared to the ECG data. Power spectrum density analysis of the electrode-skin relative movement showed that this was not the major reason for motion artifacts in ECG. For contact pressure, the motion artifacts in the ECG was reported to be closely related as a result of skin deformation. Monitoring pressure parameters for adaptive filtering is advised for future research.

Izzetoglu et al. (2005) investigates the feasibility of applying the Wiener Filtering method towards motion artifact cancellation in NIR signals. As opposed to adaptive filtering approach, the filter described does not require additional sensors and hardware configuration to the measurement system. Instead of auxiliary sensory data to estimate filter coefficients, the proposed method uses statistical data of the noise contaminated signal. The reported results show better signal to noise ratio than other adaptive methods. The objective of the Wiener filter is to minimize the square error between the true NIR signal and the estimated signal. The disadvantage with the reported method is that it require a complete set of data, which Kalman filtering is proposed as a solution.

Tong et al. (2002), like Choi et al. (2007), suggests an adaptive approach in artifact cancellation, but applied to ECG instead. Utilizing electrode motion as reference for motion artifacts, three different protocols for inducing artifacts were tested: pushing on the electrode, deforming the skin around the electrode, and pulling the lead wire. Two different sensors for motion artifact detection was attached to its respective ECG sensor. It was concluded that with either of the two, motion artifacts were reduced when used as input in the adaptive filter for the ECG.

Seyedtabaii and Seyedtabaii (2008) purpose Kalman filter for motion artifact removal in non-invasive monitoring of blood oxygen saturation, as well as heart pulsation. The primary photoplethysmograph (PPG) sensor measures both the PPG signal and the motion artifact, while strain gauges, accelerometers and Ag-AgCl paste electrodes are used as auxiliary sensors for motion artifact measurement. For reference, a system of 4 poles are generated to represent the PPG signal, while the motion artifact is a nonlinear static function, approximated by a 2nd order polynomial. The reported results show that the Kalman filter successfully reconstructs the original signal, and suppresses the artifacts.

Wood and Asada (2006) reports of heart rate estimate error of less than 1.6% using Widrow's Active Noise Cancellation algorithm in PPG measurements. The method requires a reference signal for the motion artifact, and the referenced signal must be uncorrelated to the desired signal. The PPG measurements, much like the NIR spectra, is inflicted by several factors in regards to intensity measurements, such as: ambient light intensity variation, LED/photodiode contact pressure/angle variation and motion induced blood flow and tissue alterations. Using data from a MEMS[1] accelerometer, the motion artifact reference signal is obtained, and is used recursively in a parameter tuning formula, making up the active noise cancellation. To be able to recreate the original heart beat, another sensor is needed, attached to a stationary hand.

[1] Microelectromechanical systems: microscopic devices containing both electrical and moving parts

1.4.4 Recording forces exerted from the skin

Forces exerted from the skin towards a wearable device or prosthetic socket may influence the measurements and/or performance done by the equipment. These forces may originate from skin stretch due to muscles movement beneath, as well as movement relative to the skin. When it comes to prosthetic control, the surface electromyography (sEMG) electrodes are the most common used interface towards the skin. The electrodes measure electrical potentials generated by muscle contraction, and is then used as input for the prosthetic hand/limb. As these electrodes are mounted on the skin, they rely on good contact to minimize movement artifact noise and accurately capture the subjects intentions (Li et al., 2012).

Another approach to classify movement intentions for transradial amputees, is through force myography (FMG). Wininger et al. (2008) term's FMG as "*... the radially directed muscle pressures relating to the force produced by the contractile components as well as the corresponding series and parallel elastic components within the limb*", which is interpreted as the pressure changes felt on *stratum corneum* (skin) from forces generated by muscle contractions/movement. The method is proven to give satisfactory results in classifying different hand movements and grips (Radmand et al., 2016; Li et al., 2012; Cho et al., 2016).

In Radmand et al. (2016), the possibility of using the pressure patterns from the forearm skin as primary source of prosthetic control is investigated. The muscles used to move the hand is either bulging outward or receding inwards with respect to prosthesis socket, and thus produces pressure patterns against the socket. The prototype socket developed consists of 126 custom made force sensing resistors, placed in a 14x9 High Densitiy FMG grid. The reported results show that the mean overall error in classification of hand motion was as low as 0.33%, and that HD-FMG is a potential candidate towards prosthetic control.

Cho et al. (2016) studies the classification accuracy of the FMG on the residual limb compared to the still intact limb using a strap consisting of 8 embedded FSR's. Different grips that are considered to be functional and highly useful in daily living are tested with the strap first attached to the sound limb for training. The strap is then attached to the residual limb, and the grips are repeated. FMG is reported to have an accuracy of $\sim$70% for some of the most important grips, and by subdividing the grips into two different thumbs modes, up to 89% classification accuracy were achieved using the FSR strap.

Another study of FMG/pressure distribution map feasibility is done by Li et al. (2012). Different finger motions are recorded using strain gauges at the finger tips, and a prototype socket with 32 force sensing resistors (FSRs) is attached to the anterior and posterior forearm of the subject. For six test subjects, well above 90% classification accuracy was achieved for seventeen different finger motions using the pressure distribution map from the forearm. It is shown that the FMG method gives satisfactory results for reliably distinguishing control intentions from the pressure distribution given by the forearm muscles.

1.5 Initial thoughts for solutions

This section is cited from Nøstbakken (2016), with some modifications and new additions. It is included to show possible ways to implement an auxiliary sensor for measuring the motion artifacts affecting the BioMKR device.

1.5.1 Pressure sensors between the skin and device

With one or more force sensitive sensors between the skin and casing (as done in Radmand et al. (2016)), a very direct measurement is possible to achieve. Since the sensors are in contact with the skin, the measured force is the actual skin pushing against the sensing area. The pressure is then given by

$$P = \frac{F}{A} \tag{1.2}$$

where, F is the force and A is the active area of the sensor.

The new components needs to comply with Bio compatible ISO-standard (ISO-10993-5,-10,-11 (ISO 10993-1:2009, 4)). There must also be more holes for wiring, which can compromise water and dust proofness of the wearable device (Ingress Protection IP67 (Wikipedia, 2017a)).

1.5.2 Spring loaded bioimpedance electrodes

The bioimpedance electrodes may be fitted with springs to enable movement, and measure the force as a function of displacement. With measured displacement Δx and known spring stiffness k, the force can be calculated with

$$F = k\Delta x \tag{1.3}$$

This can also be calculated to pressure as stated in Equation (1.2). Figure 1.2 shows a simple implementation. Here it might be a good idea to use four springs and calculate the average. Since the electrodes needs to be able to move, this can compromise water and dust proofness. In the original design, these electrodes are glued in place, and this method could also affect the bioimpedance reading.

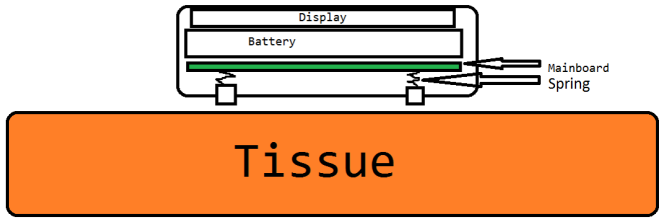

Figure 1.2: Spring loaded bioimpedance electrodes

1.5.3 Air-filled tube with pressure sensor on mainboard

A small air-filled tube that run on the underside of the device, partially inside the casing can measure the force applied by calculating the change in air pressure inside the tubing. As illustrated in Figure 1.3, a pressure sensor sits underneath the mainboard connected to the tubing. Connecting the NPC-410 pressure sensor from Amphenol (2014) to the tube, the pressure changes in the tube affects the bend of the diaphragm inside the sensor. There are strain gauges in a Wheatstone bridge configuration embedded in the diaphragm. Strain gauges suffers a tensile or compressive strain as a result of mechanical deformation in the longitudinal direction of the conductive pattern. The bend of the diaphragm affects the resistance in these strain gauges. This change in resistance affects the balance of the Wheatstone bridge, and can be used as a measure of force.

By using a dark material for the tube, as well as making it extend a few millimeters outside the casing, it can help to block external light pollution to the photo sensor. The tubing for this needs to comply with ISO-10993, as well as the hole for pressure measurement might compromise IP67.

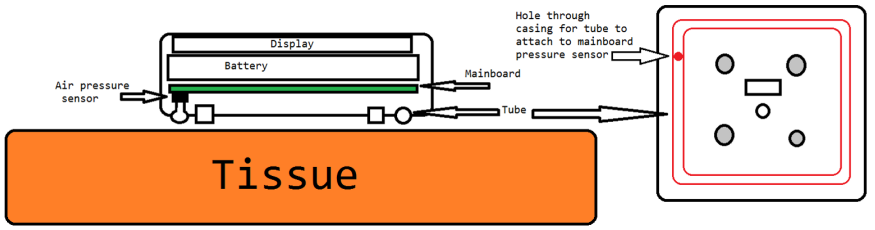

Figure 1.3: Air-filled tube with pressure measurement

1.5.4 Pressure sensor between top and bottom casing with elastic material enabling movement

The device is strapped to the arm of the wearer, where the strap is connected to the upper part of the casing. By modifying the casing with an elastic material between the top and bottom parts, the bottom part will exhibit increasing force from the top part with tighter tensions. With a small pressure sensor inside the casing, we can be able to get a different pressure reading with different tensions of the strap, as well as when external force is applied to the device. Schematic can be seen in Figure 1.4, and one or more pressure sensors can be incorporated. With more than one sensor, either each sensor can be looked at separately or the average can be calculated. The elastic material lies in between the upper and lower parts, on the outer perimeter of the device.

It is also possible to use other methods rather than just resistive force sensors. The elastic material could be a dielectric element in a capacitor, where two metal plates (electrodes) are placed on either side of the material. The change in distance

between the electrodes will alter the capacitance according to Equation (1.4), and could be a measure for force.

$$C = \epsilon \frac{A}{d} \tag{1.4}$$

where,

- C: capacitance (F)
- A: overlapping area of electrodes (m^2)
- ϵ: permittivity of dielectric material ($F \cdot m^{-1}$)
- d: distance between electrodes (m)

Using electroactive polymers as elastic space material could also be investigated. A recent review from Wang et al. (2016) evaluates the different types as sensing material for mechanical stimuli.

The drawbacks for these methods are space limitations inside the device, as well as modifications to the casing. While one of the advantage is that all components are located inside the casing, which makes complying with ISO-10993 much easier.

This method was pursued in Nøstbakken (2016), using FSRs in an empty casing.

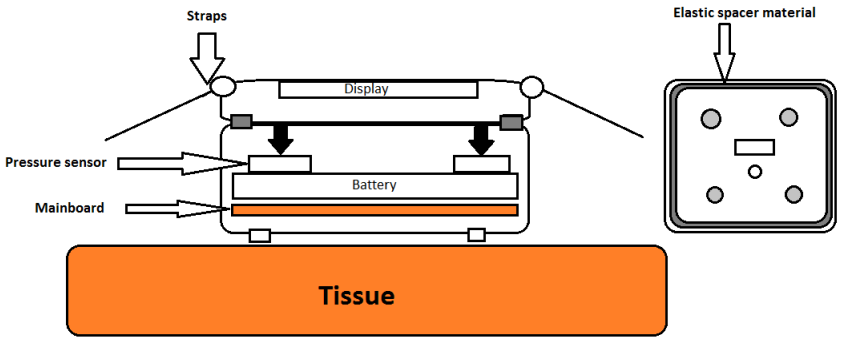

Figure 1.4: Elastic spacer material enabling movement. Sensor location in drawing is not final, and is not limited to be on top of battery.

1.5.5 Force measurements through actuator interface

Modifying the casing bottom with a new hole with rubber seal and plastic actuator, a force sensor can be placed against an IC on the PCB in the BioMKR, or the PCB itself. This only requires the actuator to be able to move, and not the entire top casing as in the previous suggestion. Although, it requires the actuator and rubber seal to comply with ISO10093, as it will lay against the skin for a longer period of time. Another drawback for this solution is that the PCB must be able to handle all forces subjected to the sensor, which could affect both NIR and Bio impedance measurements. Sensor size and additional circuitry may also be of concern.

Figure 1.5 shows the schematic for the concept that is investigated in this report, where the force sensor is laid with its back against an IC.

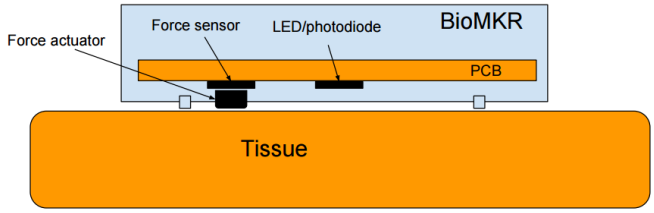

Figure 1.5: Force actuator through underside of casing.

1.6 Alternative sensors to FSR

It is suggested in Nøstbakken (2016) that other sensors with low profile for recording forces/pressure should be investigated, and the alternatives are evaluated according to signal repeatability and stability, as well as ease of use with a battery powered device.

1.6.1 Velostat Conductive Sheet

Due to its thickness, customizable size and accessability, the Velostat/Linqstat is a conductive sheet that might be a good candidate to place either inside BioMKR or between the skin and BioMKR, and is therefore evaluated.

Velostat is a pressure sensitive conductive sheet which behaves similar as a variable resistor. The sheet is only 0.1mm thick, and its resistance decreases in response to applied pressure. There is little instructions on how to properly use the sheet, but Adafruit.com lists some technical details:

Thickness: 0.1mm

Temperature limits: -45° to +65° Celsius

Surface Resistivity: $< 31\text{k}\Omega$ per square cm

The conductive sheet is highly customizable when it comes to sensor size, and can be cut in the desired size or shape. To make the sensor, the Velostat should be sandwiched between two pieces of conductive materials, either its conductive thread, copper tape or stripped/non-isolated wire. To measure the resistance change when applying pressure, the two conductive layers need to match up on either side of the pressure sensitive sheet to allow current flow.

The conductive sheet has been cut into 1cm x 1cm samples, and stripped wire has been applied in a meandering shape where the opposing wire is shifted 90° to easier achieve spots of overlap, and held together by electrical tape.

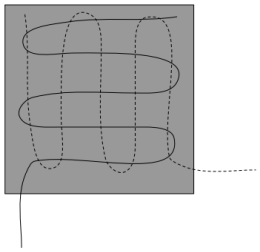

(a) 1cm x 1cm test specimen

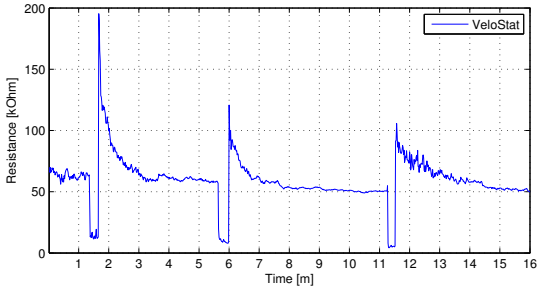

(b) Response to applied pressure

Figure 1.6: Testing the Velostat

Time [m]	Mean (Ω)	st.d (Ω)	CV (%)
0-1	63 550	3238	5.10
3-5	60 882	1660	2.73
8-10	52 295	926	1.8
14-16	53 543	2545	4.75
0-16	59 462	18 540	31.18

Table 1.1: Mean, standard deviation (st.d) and coefficient of variation (CV) from Figure 1.6b

The response from the test specimen seem to be very unstable. Without any load, the response is fluctuating with ±5kΩ. When there is applied pressure, the resistance decreases very fast, and the response is really sharp. When relieving the pressure from the sensor, it exhibits a quite drastic overshoot, to almost two-three times of what the resistance was before pressure was applied. It then takes some time (∼2 minutes) before it settles at the same level as previous.

For the stability test presented in Figure 1.7, the Velostat is fluctuating around R = 49 602±1047Ω with a CV of 2.11%. The sensor is resting mid air on its own conductive wires on an elevated surface, so that there is nothing touching either side of the Velostat. Due to the lack of documentation available, the building of the sensor as well as testing its response is a procedure of trial and error. This makes it hard to know if it is done correctly.

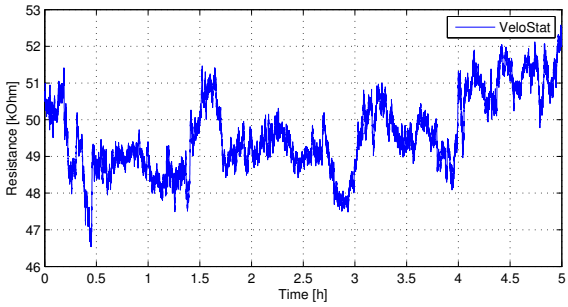

Figure 1.7: Stability test, Velostat

The advantages for using the Velostat are that it is highly customizable, cheap and easily accessible, while the drawback is its lack of documentation, leading to inaccurate readout, low repeatability and poor quality configurations from guesswork.

Although some unstable response, we wanted to see how the output looked if we covered the entire underside of the device with the conductive sheet. Holes were cut in the specimen for NIR measurements, and the sensor was constructed using stripped wire laid in a meandering shape. The test is a simplified version of the strap test presented in Nøstbakken (2016), and which will be stated later in this thesis (Section 2.4.3).

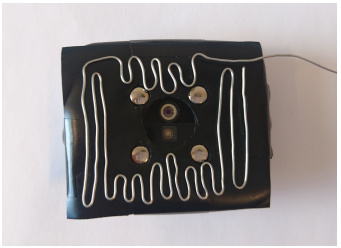

(a) Velostat underside BioMKR, first layer

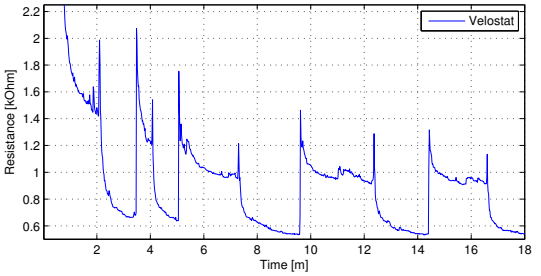

(b) Strap tension from light to max tension

Figure 1.8: Testing the configurability of Velostat.

The output signal is similar to some degree, but with almost two minutes between tension variation, the signal is still not stabilized.

1.6.2 EeonTex Pressure Sensing Fabric

Similar to the Velostat, a pressure sensitive fabric with low profile is evaluated for the use in BioMKR.

Another conductive material with piezoresistive properties is a nonwoven fabric made by EeonTex. The pressure sensing fabric NW170-SLPA-2k exhibits decreasing resistance as a result of pressure, and can be cut in desired size and shape. Similar to the Velostat described previously, the response is determined by the amount of contact points from the conductive leads on either side of the fabric.

Thickness: 0.8mm

Temperature limits: -40° to +100° Celsius

Surface Resistivity: 2kΩ per square cm

(Information from (EeonTex))

The testing of this fabric is also cut into 1cm x 1cm specimens, where stripped wires are laid in a meandering shape, as shown in Figure 1.6a. The response is very similar to the one from Velostat. It reacts as soon as pressure is applied, where its resistance drop by several kΩs (see Figure 1.9). The same overshoot and settling time as Velostat is seen for the fabric, but this might be because of similar build with stripped wire and electrical tape making up the sensor. The fabric seem to have higher hysteresis than Velostat, as it finds a higher resistance level after pressure is relieved.

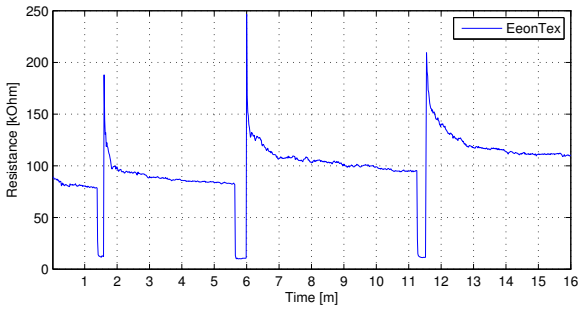

Figure 1.9: Response to applied pressure, EeonTex

Time [m]	Mean (Ω)	st.d (Ω)	CV (%)
0-1	82 609	2603	3.15
3-5	86 235	1649	1.91
8-10	101 756	2145	2.11
14-16	111 413	993	0.81
0-16	99 004	26 888	27.16

Table 1.2: EeonTex response to light pressing and releasing actions

For a stability test (see Figure 1.10), the sensor is resting its conductive leads on an elevated surface such that neither of the sides of the sensor is receiving physical contact. The fabrics resistance varies with R = 96 276±1964Ω and CV = 2.04%. Looking at $CV_{Velostat}$=2.11% vs EeonTex, there really is no difference in performance for a non actuated test sensor. For the response test presented in Tables 1.1 and 1.2, the EeonTex has some better performance concerning signal stability.

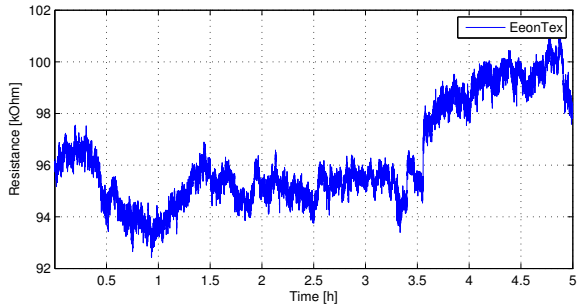

Figure 1.10: Stability test, EeonTex

The advantages and drawbacks for using the EeonTex pressure sensing fabric are much like the Velostat, except that it is 8 times thicker.

1.6.3 FlexiForce A101 Force sensor

Similar to the FSR used in Nøstbakken (2016), the piezoresistive property is used as a measure of force exerted on the sensing area of the FlexiForce sensors from Tekscan. The sensor exhibits a decrease in resistance as a response to the applied force. It is a flexible printed circuit constructed of two layers of polyester film substrate. Each substrate is coated with a conductive material and pressure sensitive ink, and when load is applied to the active area of the sensor, the two substrates comes into contact leading to a decrease in resistance. (Tekscan, 2010).

Active area	Ø3.8mm = 11.34mm^2
Length	15.6mm + 6mm solder tabs
Width	7.6mm
Thickness	0.203mm
Connection	Solder tabs
Repeatability	$< \pm 2.5\%$ of full scale
Hysteresis	<4.5% of full scale

Figure 1.11: FlexiForce Model A101 (from Tekscan datasheet)

One option for circuit configuration is to connect the FlexiForce to an inverting amplifier with a fixed reference/feedback resistor (R_F) and a negative driving voltage (V_0). The FlexiForce behaves like a variable resistor (R_{A101}) and the circuit output can be evaluated according to Equation (1.5). The sensitivity for the setup is adjusted by replacing the feedback resistor R_F

$$V_{out} = -V_0 \cdot \frac{R_F}{R_{A101}} \tag{1.5}$$

The reported characteristics are quite good, with its sensor size, ease of use and being designed to be embedded into products and prototypes, the FlexiForce A101 makes a good candidate to be tested in conjunction with the BioMKR.

Vecchi et al. (2000) have evaluated the FlexiForce Model A201 and Interlink Electronics' Model 402 through a series of experiments and compared the performance with respect to linearity, repeatability, drift and dynamic accuracy. The FlexiForce performs better, but lacks robustness, as one of the sensors broke after repetitive actuation for the sensor. Robustness is important when evaluation options for the BioMKR, and components should have a lifetime of >2 years (Nøstbakken, 2016).

1.6.4 Honeywell FSA Series

Honeywell Sensing and Internet of Things has a wide variety of sensors, including force sensors for various applications. Nøstbakken (2016) evaluates the FSS Force sensor where a steel ball is pushed down to a silicone-sensing element connected to a Wheatstone bridge. As of 2017, Honeywell released a new piezoresistive-based force sensor available with both analog and digital output(FSA Series) (HoneywellSensing, 2017). Some of the features are listed below:

Force range (N): 5, 7.5, 10, 15, 20, 25

Accuracy: ±3 %

Supply voltage: 3.3 Vdc or 5.0 Vdc

Digital communication: SPI or I^2C

Temperature range: Fully calibrated and compensated from 5 °C to 50 °C

Figure 1.12: Honeywell FSA (from HoneywellSensing (2017))

The actuation system is a circular platform with diameter Ø = 12.70mm, as opposed to the FSS' steel ball actuator. The drawbacks for this is its bulky design, with a width of 7.36mm and total length of 31.5mm the space inside BioMKR quickly become a problem. The BioMKR do have a corner where the circuit board does not fully extend, and would be the only option for placement of this sensor.

1.6.5 Choosing the sensor

When it comes to sensor choice, again we land on Interlink Electronics' FSRs. This is because of their ease of use, compact design, available documentation, experience from earlier work, as well as availability.

It is suggested from Nøstbakken (2016) that the FSR should be tied to a measurement circuit in a voltage divider setup, and by selecting the other components of this circuit, a more linearized output is believed to be expected from the FSR ((Interlink Electronics, 2013)). A more detailed description of the characteristics of the FSR of choice will be presented in Section 2.1.3.

Chapter 2

Materials and Methods

2.1 Equipment

2.1.1 USB DrDAQ data logger

The USB DrDAQ Data Logger developed by Pico Technology LTD is a compact and multifunctional transmitter which features 16 different channels for observing measurands and outputs, connected to the USB port of any computer. The connections of interest are the EXT-channels as well as the Scope channel. For more details see (Pico Technology, 2016; Nøstbakken, 2016).

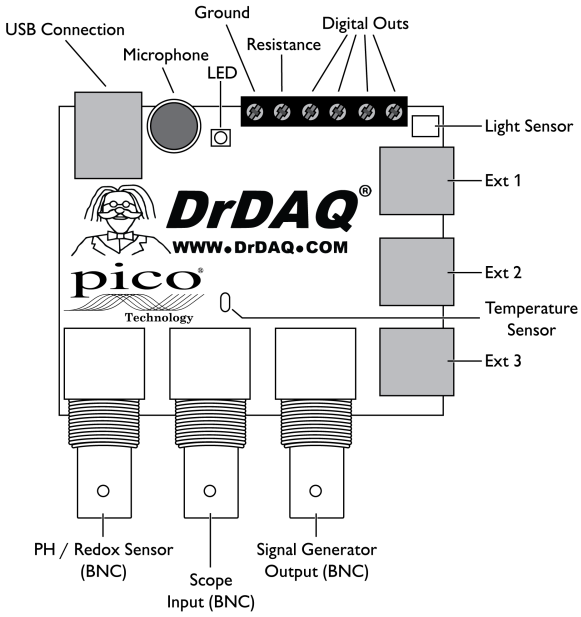

Figure 2.1: Overview of the connections. (From Pico Technology (2016))

Oscilloscopes are used for evaluating circuits and components and their electrical characteristics with respect to voltage amplitude, signal rise time, frequency and so on. The USB DrDAQ has a channel called Scope, where it is possible to connect a probe with a BNC-connector.

Signal Type:	Input
Range	Bidirectional: ±1.25V, ±2.5V, ±5**V**, ±10V
Resolution	8 bit
Accuracy	3%

2.1.2 Data logging software

The DrDAQ comes with PicoScope 6 software for evaluating the input to the data logger, as well as additional software (PicoLog Recorder/Player) for experiments over longer periods (e.g. night test). The results presented by Nøstbakken (2016) was gathered by these programs. Due to erroneous values logged, it was recommended that further evaluation with DrDAQ and/or FSR should be done with a different software, in which we decided to write our own. The program was written in Java and was suggested by Prediktor, due to their expertise in the environment.

The software designed is a simple tool developed to continuously write data to .txt files both locally and backup to cloud. With real time plotting of the data, it gives good visual representation of the performance for the selected measurement. To be able to communicate with the DrDAQ data logger, it needs a dynamic link library file (.dll, provided by the engineers at Prediktor) as well as a native library file (.lib, provided by Pico Technologies). Figure 2.2 shows the essentials of the program. The source code will be provided as a separate .zip-file upon submission.

Workstation specifies the directory path for where the log file should be saved to, both locally and for cloud synchronization.

Compare data states whether or not the raw 'float' data, the processed 'doubles' data as well as the rounded 'String' data should all be logged for comparing the differences. This option was mostly used during troubleshooting signal quality, as will be more discussed in Section 2.3.

Timescale converts the **Duration** specified by the user to the correct amount of samples corresponding to 1 sample per second.

Average shows the average value for the session.

When the session is over, the software saves a .PNG of the graph in the directory paths given by Workstation. Hitting **close** exits the window and terminates the session.

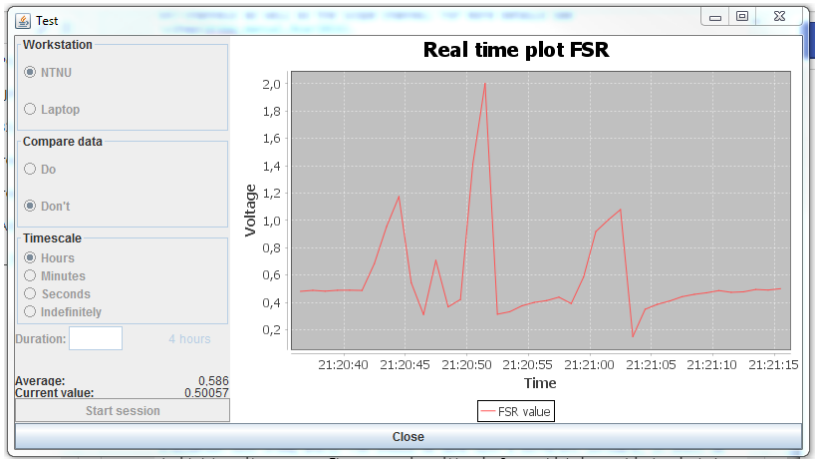

Figure 2.2: Java logging interface

2.1.3 Force Sensing Resistors

Force Sensing Resistors (FSRs) use the electrical property of resistance to measure force applied to the active area of the sensor. The sensor consists of two membranes and a plastic spacer. The bottom substrate is coated with a carbon-based ink, making it conductive. The top layer consists of two sets of interdigitated circuit patterns, forming the active area of the sensor. A plastic spacer separates the top and bottom layer, forming an air gap between the substrates. Both substrates are normally made by polyethylene terephthalate (PET) (Interlink Electronics). Figure 2.3 shows the two layers, broken apart and laid partially over each other.

When an external force is applied against the active area of the sensor, the two layers are pushed toward each other. When the bottom conductive layer shorts the interdigitated patterns, the resistance between the conductive fingers decreases with increasing force. An actuation force (or break-force) is the minimum amount of force needed to make contact between the two layers, and break the sensors idle state(R_{fsr}^{idle} >10MΩ). This will bring the sensor into the sensitive measuring range (R_{fsr}^{max} to R_{fsr}^{min}). For this project, Interlink Electronics' FSR400 Short is used.

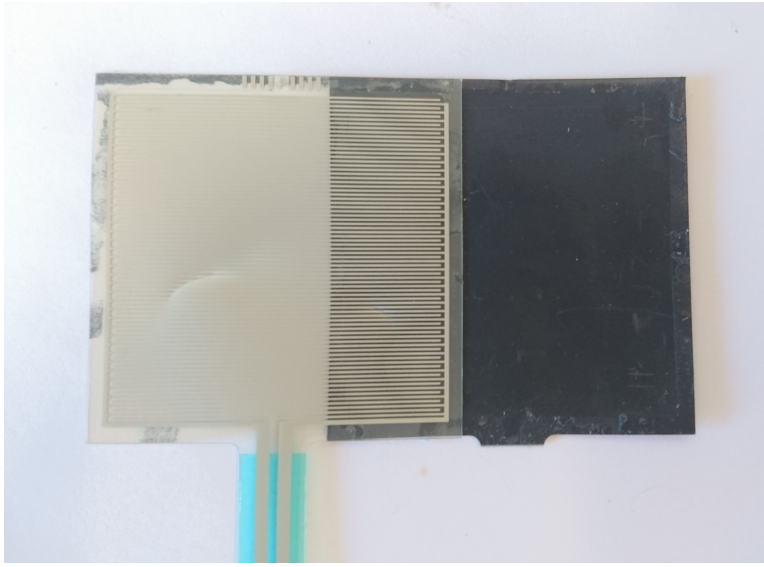

Figure 2.3: The two layers of an Interlink Electronics FSR406

Active area	Ø5.62mm = 24.63mm^2
Length	15.8mm ± 0.15
Width	6.35mm
Thickness	0.30mm ± 0.03
Connection	Solder tabs
Force range	∼0.2N - 20N
Repeatability	±2%
Hysteresis	+10% average resistance change

Figure 2.4: FSR400 Short tail (From DigikeyElectronics)

2.1.4 BioMKR

The BioMKR device has a light emitting diode (LED) array consisting of 10 LEDs emitting NIR light with peak wavelengths ranging from 905nm to 1720nm. A photodiode in near proximity picks up the reflected light. The LED array and photodiode are separated by an optical barrier to eliminate specular reflection. Additionally, the device have two injecting and two pick-up electrodes, making up the Bio impedance measurement circuit. The injecting electrodes inputs a current signal to the tissue, and the gain/phase response is measured by the two opposing pick-up electrodes. For the Bio impedance circuit, frequencies from 10kHz to 25MHz are used.

Device temperature, accelerometer as well as photodiode response when no LED is on, provide valuable information considering device performance and signal interpretation. The latter parameter is a measure of external light, and is characterized as *NIR Dark* in the BioMKR.

Two BioMKR devices have been used in this report: Prototype I and Prototype II. Prototype I is a device based on BioMKR revision C, and consists of an FSR sandwiched in between an IC and a modified actuator. For the readout of the force signal, an external circuit as will be described in section 2.2 is connected to the DrDAQ data logger. Preliminary evaluation of FSR response and verifying FSR/Prototype I functionality was recorded using the software presented in Section 2.1.2. For tests involving BioMKR measurements (NIR, internal temperature etc.), software and cloud services provided by Prediktor was used.

Prototype II is based on the revision E BioMKR device. It has a customized bottom casing and a measuring circuit for the FSR has been incorporated on a small PCB. It also has an FSR sandwiched between the bottom and an IC on the mainboard. The actuation of FSR is done with a plastic actuator and rubber seal, and is one of the major mechanical changes from a ordinary BioMKR device. Retrieving BioMKR data as well as FSR data was done through software and cloud services supplied by Prediktor.

2.1.5 Prototype I description

The engineers from Prediktor suggested that the FSR should be placed on a specific IC due to the space limitations inside the device. There was ordered new casing bottoms from their supplier to enable FSR actuation through the casing. Similar modifications was done to the rev.C device, making what will be referred to as Prototype I from now on. With the help from the mechanical workshop at the Department of Cybernetics, a new hole was milled to fit another impedance electrode to work as an actuator. An impedance electrode was milled and modified to have a flat interface towards the sensitive area of the FSR. A hole on the side of the casing was cut to allow the FSR tail and solder tabs to stick out of the device and enable connectivity of the sensor (see Figure 2.5a). The screws where tightened and V_{out} was read to confirm functionality.

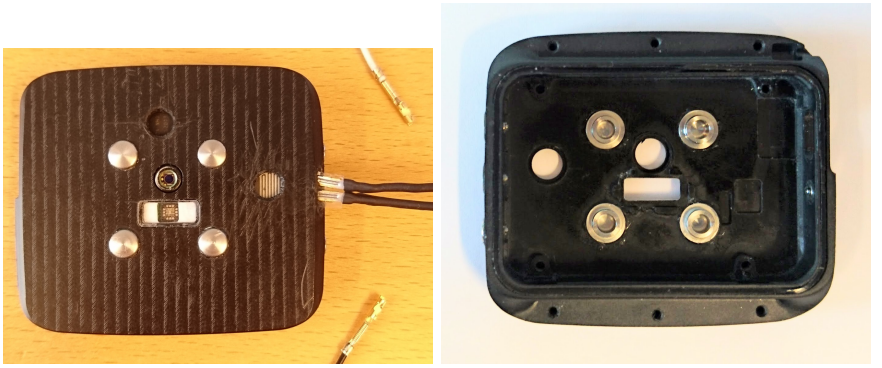

(a) FSR visible to the right **(b)** Hole milled for FSR actuation

Figure 2.5: Prototype I modifications

Figure 2.6: Impedance electrode modified to be the actuator

2.1.6 Prototype II description

The second prototype, designed by the engineers at Prediktor, introduce a new interface towards the skin, as well as an additional PCB with the circuitry for the FSR measurements. The plastic actuator seen on the right in Figure 2.7a is designed to be able to pick up the forces felt by the device from the skin. The FSR circuit is connected to a spare ADC channel on the BioMKR PCB and the data captured is stored in flash memory. This memory is of finite size, and can hold up to $\sim$ 4 hours of data. When this limit is reached, old data points gets overwritten.

(a) New actuator visible to the right

(b) Inside of Prototype II bottom casing with actuator visible to the left

Figure 2.7: Prototype II modifications

2.1.7 NIR signals from the prototypes

The NIR signal picked up by the photodiode in the BioMKR devices has been subjected to absorption, scattering and reflection from the tissue. This signal is not further calculated and transformed to diffuse reflectance as done by others (e.g. (Chen et al., 2005; Chan et al., 1996; Reistad et al., 2015; Cugmas et al., 2014)), and the wavelength data retrieved from the device is the output voltage from the photodiode measurement circuit. In this thesis, the terms *NIR signal(s)* and *NIR value(s)* will be used to address this signal, and *Photodiode output* will be used when labelling graphs.

Improvement of actuator

The Prototype II from Prediktor showed little to no response in regards to force readings when worn on the arm. This was due to two factors:

1. The space between the actuator and FSR was too big
2. The plastic actuator had too small geometric shape in regards to indentation and diameter

The first issue was improved by adding a round, 0.5mm thick plastic material on the inside of the BioMKR, between the actuator and FSR.

The interface towards the skin needed to be redesigned. This was done by first drilling a 0.5mm hole into, but not through, the plastic actuator. A total of 5 adapters of various sizes and geometrical shapes were made in plastic material, with a "foot" to fit the hole in the original actuator for support.

Three types with 1mm thickness and flat surface have been evaluated:

1. Round, diameter = Ø13mm,
2. Round, diameter = Ø8mm,
3. Rectangle, length = 30mm, width = 4mm

In addition, two adapters with thickness = 0.5mm and diameter = Ø13mm was produced: conical form and flat surface. Table 2.1 lists the properties and gives a unique identifier for each adapter.

Shape	Diameter (Ø,mm)	Max thickness (T,mm)	Length (L,mm)	Width (W,mm)	Identifier
Round	13	1.0	-	-	Ø13T1.0TEST
Round	13	1.0	-	-	Ø13T1.0FLAT
Round	8	1.0	-	-	Ø08T1.0FLAT
Round	13	0.5	-	-	Ø13T0.5FLAT
Conical	13	0.5	-	-	Ø13T0.5CONE
Rectangular	-	1.0	30	4	L30W4T1.0RECT

Table 2.1: Adapters

The different adapters have been evaluated according to:

- FSR response and stability
- Skin indentation, irritation and general comfort
- NIR Dark change
- NIR signal perturbation

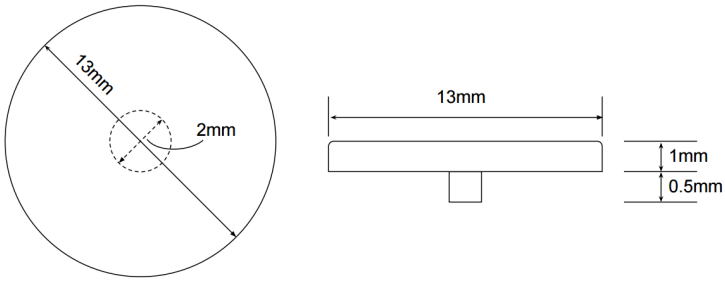

(a) 13mm round adapter, 1mm thickness

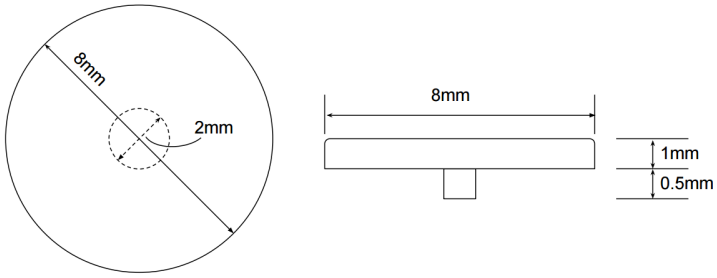

(b) 8mm round adapter, 1mm thickness

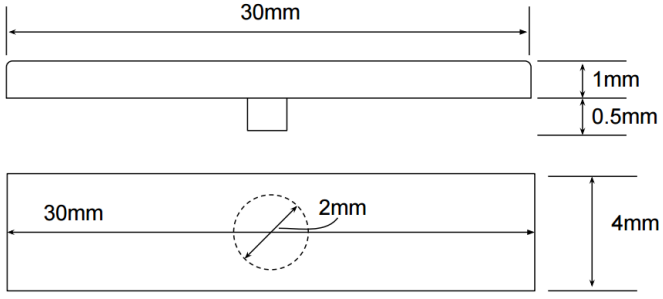

(c) 30mm square adapter, 4mm width, 1mm thickness

Figure 2.8: Concept drawings of the adapters

2.2 Circuit design

As stated in (Nøstbakken, 2016; Interlink Electronics, 2013), it is recommended that the FSR is used in conjuction with a measuring resistor R_M in a voltage divider. If the measurement device have a high impedance input, the circuit can be followed by an operational amplifier (OpAmp) (Interlink Electronics, 2013) . A rule of thumb for selecting pull-up resistors, is making it 1/10th of what the input impedance is (Sparkfun, 2017). Since the EXT-channel have a 100kΩ pull-up to 2.5V, there is reason to believe that the input impedance is greater than 1MΩ, making it "high impedance", and therefore an OpAmp is used in this setup.

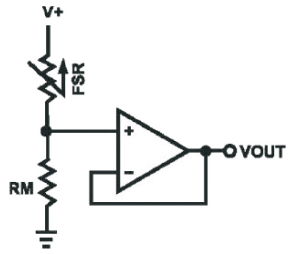

Figure 2.9: FSR voltage divider (From Interlink Electronics (2013))

The voltage measured at V_{out} from Figure 2.9 can be explained as:

$$V_{out} = \frac{V^+ R_M}{R_M + R_{FSR}} \tag{2.1}$$

where V^+ is the input voltage source powering the circuit.

With decreasing resistance over R_{FSR} upon increasing force, the output voltage V_{out} is increasing.

The OpAmp is a LM324 low power quad operational amplifier produced by STMicroelectronics (STMicroelectronics, 2011). It supports both single and bipolar power supply, and for this setup a single power supply of +5V is used.

2.2.1 Simulating the circuit

To see the performance of the OpAmp chosen for further investigation, Texas Instruments' TINA software is used. This electronics lab enables us to draw the schematic for a given circuit, and analyze its performance.

The analysis of interest is Transient Analysis. Transient reflects how the setup will work with time, it enables us to see how much time the output needs to reach the desired level (in response to a change at the input), and how it behaves as time passes (stability, charging/discharging profiles).

STMicroelectronics' OpAmp needs to be imported to TINA (see Section 6.1) to simulate, and the TINA Schematic for the measuring circuit is seen in Figure 2.10.

The result from the Transient Analysis can be seen in Figure 2.12a.

The OPA333 CMOS Operational Amplifier (TexasInstruments, 2006) was chosen by the engineers at Prediktor to be used when the FSR is going to be integrated with its own measuring circuit inside the BioMKR. Therefore the Transient Analysis will be evaluated for this also. The schematic can be seen in Figure 2.11.

A decoupling capacitor of 100nF is attached close to the power supply-pin of the amplifier (see Figures 2.10 and 2.11). This is to ensure smooth power to the component, in case of noisy or high-impedance power supplies (TexasInstruments, 2006).

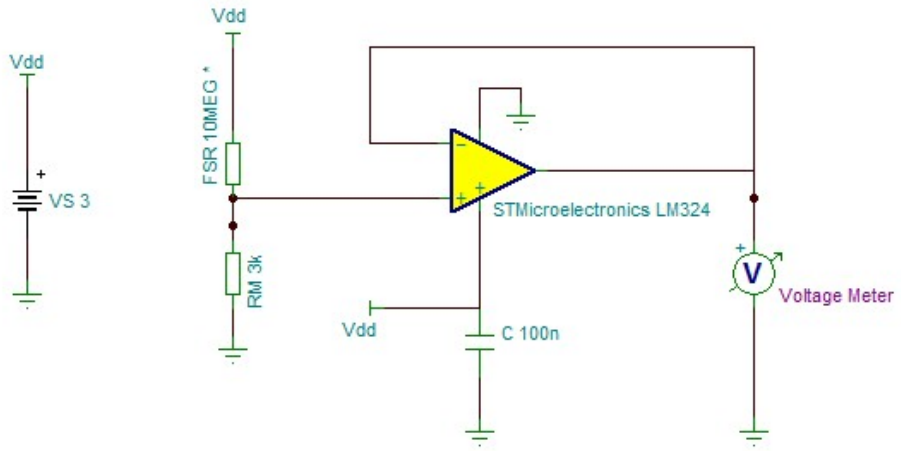

Figure 2.10: Circuit Schematics in TI TINA; LM324

R_{FSR} is set as the control object, which we define 100kΩ as start value, and 1kΩ as end value. By choosing a logarithmically sweep type with 5 different cases, the transient analysis runs through the simulation for five different values of R_{FSR}. Initially, when R_{FSR} does not exhibit any force, $R_{FSR} > 10M\Omega$. Since R_{FSR} is a trigger type sensor, a certain force is needed to bring it to dynamic range, which is between 100kΩ and 1kΩ. This is why the start value is set to 100kΩ and not 10MΩ.

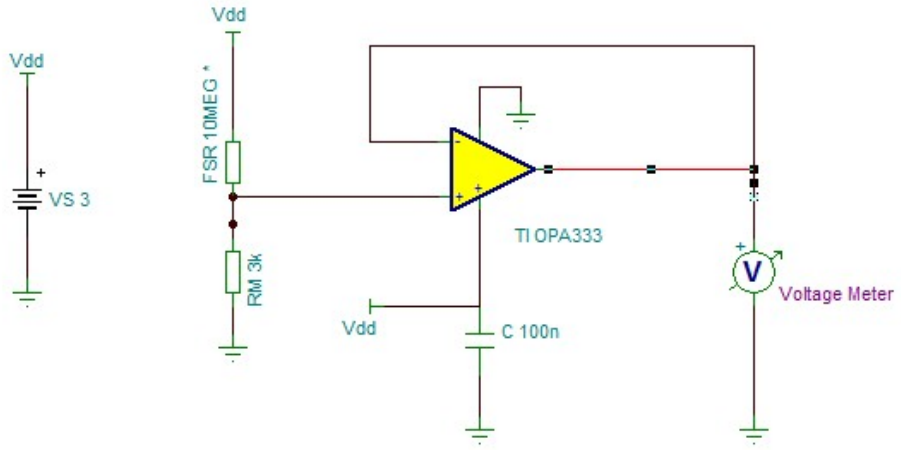

Figure 2.11: Circuit Schematics in TI TINA; OPA333

Using Equation (2.1) we calculate the expected output for each simulation case from TINA:

$$R_{FSR} = 100k\Omega = 87.4mV \tag{2.2a}$$
$$R_{FSR} = 31.6k\Omega = 260.1mV \tag{2.2b}$$
$$R_{FSR} = 10k\Omega = 692.3mV \tag{2.2c}$$
$$R_{FSR} = 3.2k\Omega = 1.45V \tag{2.2d}$$
$$R_{FSR} = 1k\Omega = 2.25V \tag{2.2e}$$

Looking at the response for STMicroelectronics' LM324 in Figure 2.12a, it uses less than $5\mu s$ to give a stable response. Although fast, it does not reach the correct, expected value for $R_{FSR} = 1k\Omega$ (see Equation (2.2)). In comparison, TI's OPA333 is slightly slower ($< 16\mu s$), but achieves correct response for the total dynamic range of the FSR (see Figure 2.12b). Although being slower, the time used is not of any concern in practical applications where sampling frequency is less than 4Hz.

From the data sheet for the LM324 (STMicroelectronics, 2011), the minimum power supply is 3V, which might be the reason for not reaching the correct value of 2.25V in the simulations. The lowest V_{dd} recorded to give correct output at $R_{FSR} = 1k\Omega$ was found to be 5.5V. For the breadboard setup, power supply is 5V, which gives a 10mV lower output at $R_{FSR} = 1k\Omega$ in simulations than the theoretical value, and should not be a problem.

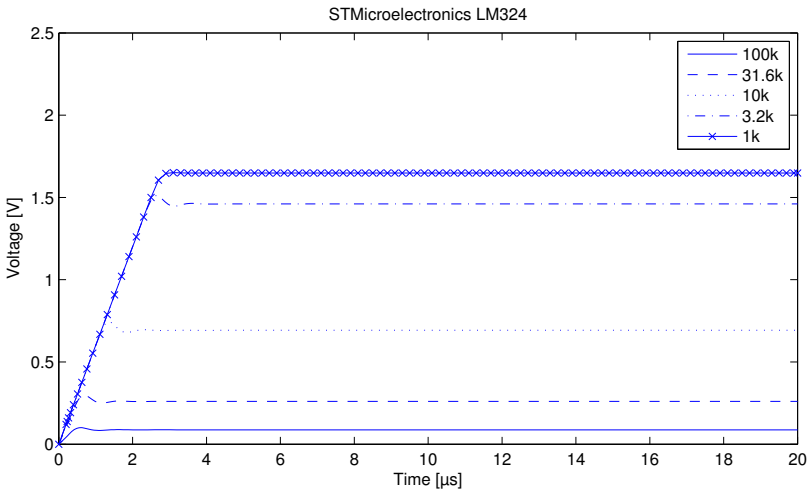

(a) STMicroelectronics LM324

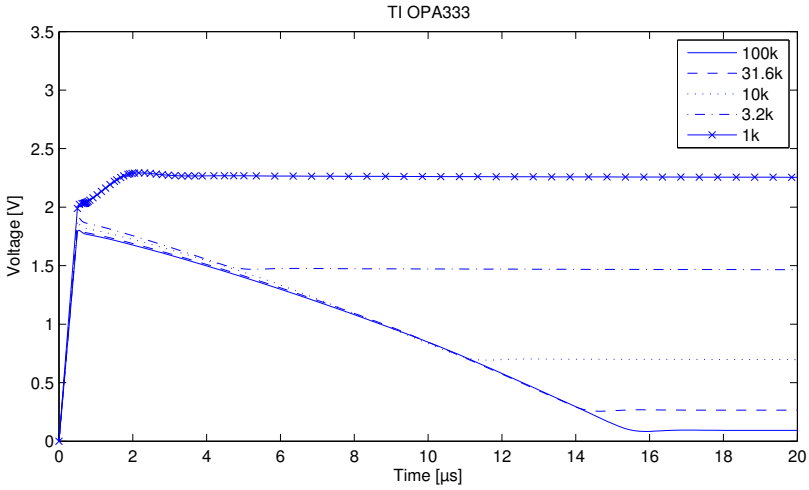

(b) TI OPA333

Figure 2.12: Transient Simulation Response

2.3 Test setup

As stated in Section 2.2, some initial circuit design testing included the LM324N OpAmp in conjunction with an FSR and measuring resistor. This setup was performed on a breadboard, with a 5V supply voltage and ground provided by one of the EXT-inputs of the DrDAQ, and $R_M = 3k\Omega$. The response was evaluated by measuring the output of the OpAmp. Immediately the output is seen to swing in an increasing manner as expected.

The dynamic *range* for the FSR is from break-force to $R_{FSR}^{min} = \sim 1k\Omega$. The break-force is the amount of force needed to bring the FSR resistance from $R_{FSR}^{idle} > 10M\Omega$ to $R_{FSR}^{max} = 100k\Omega$. This gives a dynamic range for the measuring circuit from V_{out}^{min} to V_{out}^{max}.

$$V_{out}^{min} = \frac{V^+ R_M}{R_M + R_{FSR}^{max}} = \frac{5V \cdot 3k\Omega}{3k\Omega + 100k\Omega} = 146mV \tag{2.3a}$$

$$V_{out}^{max} = \frac{V^+ R_M}{R_M + R_{FSR}^{min}} = \frac{5V \cdot 3k\Omega}{3k\Omega + 1k\Omega} = 3.75V \tag{2.3b}$$

Using the DrDAQ data logger, there are two options to measure the output voltage: Scope or EXT. Both have their advantages/disadvantages, where range and resolution are key parameters (see Table 2.2).

Table 2.2: Scope vs EXT channel specifications

	Scope	EXT
Resolution	8bit	12bit
Range	see Section 2.1.1	0-2.5V

With Equation (2.4), the LSB for both measurement options can be obtained. To achieve a highly sensitive measurement setup, this number should be as low as possible.

$$LSB = \frac{Range}{Resolution} \tag{2.4}$$

$$LSB_{scope} = \frac{\pm 5V}{2^8} = \frac{10V}{256} \approx 39.1mV \tag{2.5}$$

$$LSB_{EXT} = \frac{2.5V}{2^{12}} = \frac{2.5V}{4096} \approx 0.610mV \tag{2.6}$$

When the scope channel is evaluated using PicoScope 6 software, a Δ=27mV is observed when a stable signal is expected. In theory, this number should be closer to LSB as calculated in Equation (2.5). Either its the theoretical or observed LSB, it is not sufficient for evaluating the response.

From Equation (2.6) it is clear that the EXT channel is superior when it comes to resolution, but inferior when it comes to measuring range. Looking at Table 2.2 shows a narrow measuring range from 0 to 2.5V. As a consequence, this channel is not able to measure the upper 1.25V of the span for this setup.

Solving Equation (2.1) with respect to R_M:

$$V_{out} = \frac{V^+ \cdot R_M}{R_M + R_{FSR}} \tag{2.7a}$$

$$R_{FSR} = \frac{V^+ \cdot R_M}{V_{out}} - R_M \tag{2.7b}$$

$$R_{FSR} = \frac{5V \cdot 3k\Omega}{2.5V} - 3k\Omega = 3k\Omega \tag{2.7c}$$

As soon as the forces reduce R_{FSR} to 3kΩ, the signal reaches 2.5V and further increase in force does not yield increasing V_{out}.

Figure 2.13 shows the difference in data collected by the Scope and EXT channel over 16 hours. The FSR is situated inside the Prototype I, and the data is recorded with software presented in Section 2.1.2.

The data from Scope channel is hard to interpret. Its low resolution makes the output inaccurate, and the data logger does not limit itself to only output at levels that correspond to multiples of LSB. Instead we see a signal that varies quite much in between.

The output from EXT channel is much easier to interpret, as a result of higher resolution. The signal experiences 1.86% drift, and is similar to findings in Nøstbakken (2016).

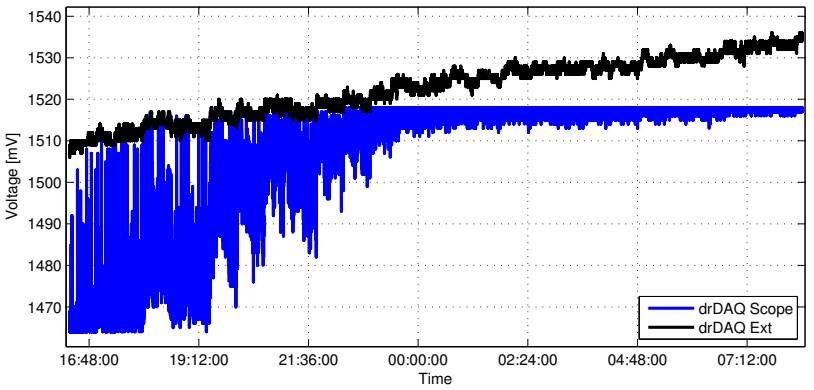

Figure 2.13: Comparison of Scope and EXT over 16hours

For further evaluation of Prototype I performance, EXT channel is chosen due to greater resolution. For real life applications where the device is worn on the arm, 2.5V is unlikely to be achieved with the current circuit configuration.

For testing with the Prototype II, the measurement system is tied up to a 12-bit ADC and a power regulator delivering 3V, and solving Equations (2.3) and (2.4) produce:

$$V_{out}^{min} = \frac{3V \cdot 3k\Omega}{3k\Omega + 100k\Omega} = 87mV \tag{2.8a}$$

$$V_{out}^{max} = \frac{3V \cdot 3k\Omega}{3k\Omega + 1k\Omega} = 2.25V \tag{2.8b}$$

$$LSB = \frac{3V}{2^{12}} = 0.732mV \tag{2.9}$$

2.4 Experiments

Prior to receiving the customized actuator adapters presented in Section 2.1.7, Prototype II was fitted with a test adapter in experiments where the device is worn.

The test adapter was hand made with a Ø13mm poly carbonate piece and a short screw through the piece as "foot". The screw is slightly longer than the depth of the actuator hole, so the adapter will stick out a bit more than the customized adapters. See Figure 2.14.

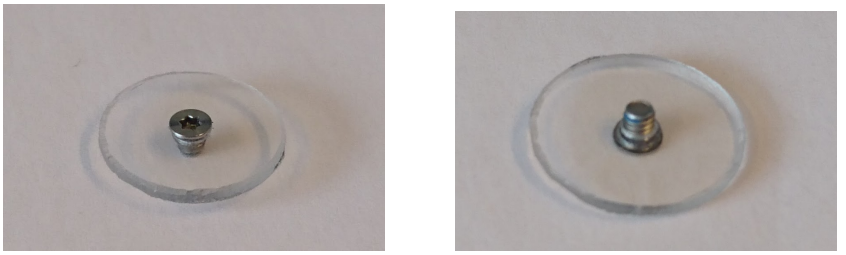

(a) Top **(b)** Bottom

Figure 2.14: Test adapter

2.4.1 NIR test block

An important thing to investigate when placing a force sensor inside the BioMKR, is how the NIR measurements are affected. Since the FSR is resting against an IC on the same PCB as the LED array/photodiode which is responsible for collecting the raw data for glucose calculations, the PCB may be subjected to some degree of bend if the force pressing on the FSR is big enough, or the distance between the FSR and holding points for the PCB are too big. To be able to test this, a test block was customized to fit the dimensions of the BioMKR. The block was milled with holes for impedance electrodes, a 15mm pit for the NIR to travel and reflect back to the sensor, as well as a hole going through the whole block to enable actuation of the FSR. There was also milled a 2mm deep socket in which the BioMKR fits to block external light. The parameter *NIR Dark* together with other parameters calculates the level of trust from other data collected by the BioMKR. For the current setup, NIR Dark$\approx$0.273, and any value below 0.3 is acceptable. A desk lamp is used to shed light onto the setup and if the photodiode picks this up, the NIR Dark value will increase. No change is seen when this is done.

The BioMKR is taped to the test block, laying face down on the desk, with the test block on top of it. A Hex Bolt A4.80 is used to actuate the interface against the FSR.

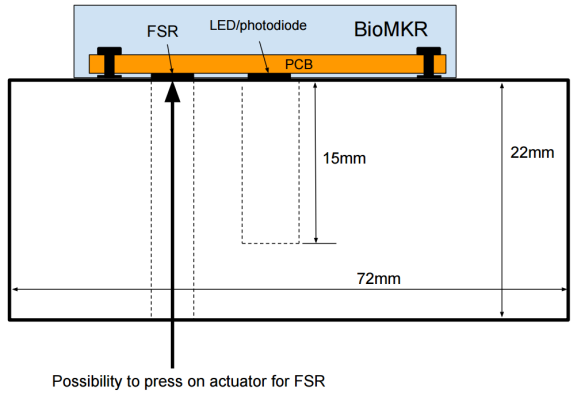

(a) Drawing of NIR test block

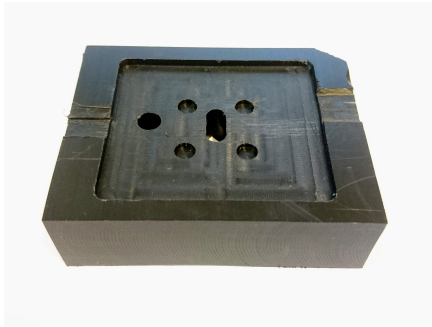

(b) Slot for BioMKR

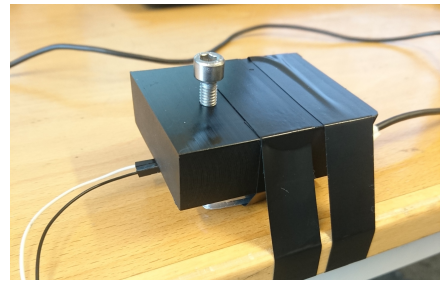

(c) NIR test setup

Figure 2.15: NIR test block

2.4.2 PCB bend test

Placing the FSR against the PCB carries a risk of perturbing the NIR signal due to movement of the NIR measurement system, caused by flexing of the PCB when force is applied to the actuator. To investigate if this is the case, a bend test was performed. Using the NIR test block described in Section 2.4.1, an incremental force test using two A4-80 stainless steel nuts and the hand was done. Although identical, the steel nuts did not weigh the same (53g and 57g). Standardized weights should be used if tests requiring higher precision is to be conducted, but for this test these nuts are sufficient.

The procedure presented in Figure 2.16 below is repeated three times.

1. Zero load (30 seconds)
2. 1 nut (30 seconds)
3. Zero load (30 seconds)
4. 2 nuts (30 seconds)
5. Zero load (30 seconds)
6. Hand push to ∼1.5V (30 seconds)
7. Zero load (30 seconds)

Figure 2.16: Incremental bend test

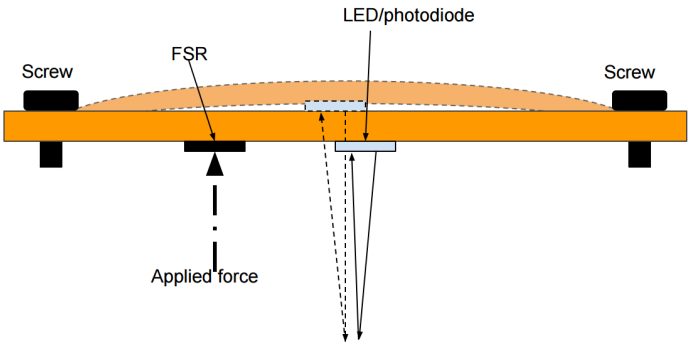

Figure 2.17: Concept drawing of PCB bend due to force

2.4.3 Strap Test

Even the slightest compression of the skin can alter the optical properties in the tissue below (Chan et al., 1996; Shangguan et al., 1998), and to investigate how the NIR measurements change with different strap tightness, a similar strap test as presented in Nøstbakken (2016) was conducted on the anterior upper arm. The signal stability and response for the different adapters for Prototype II was also evaluated. Four different tensions or grades of tightness was defined on the velcro strap:

Loose (0): Very loose, only to ensure no light pollution to NIR signals

Light (1): Light tension with the velcro strap, optimal comfort

Tight (2): Prototype tightened to replicate tight fit. Slight discomfort

Max (3): Prototype is tightened max, without ability to further tension. Discomfort

The procedure from Nøstbakken (2016) will be restated here: Start with loose tightness, and increment each minute. The arm should be supported such that it can rest horizontally without actively engaging the muscles. When max tightness has been reached, revert the procedure by slacking until loose setting is done. Repeat the procedure two times. The test was conducted with both Prototype I and Prototype II devices.

Figure 2.18: BioMKR on-body tests on anterior upper arm.

2.4.4 Night test

During the night, the subject may move limbs and/or entire body, or even roll over and lay on top of the device for a longer period of time. These events may produce significant movement artifacts to the NIR and Bio impedance signals. Prototype II has the possibility to log FSR values without connecting it to an external data logger. This enables us to do a night test where the device is strapped to the subjects arm while sleeping (see Figure 2.18). The tests were conducted with light strap tightness (1) as presented in Section 2.4.3, and with the different adapters discussed in Section 2.1.7. The tests were carried out between 00:00 and 09:00.

2.4.5 Temperature test

Temperature dependency for the FSR was reported in Nøstbakken (2016), which deviated from the expected drift from high operating temperature presented in (Interlink Electronics, 2013). To investigate if this happens for a fully functional BioMKR, and how the NIR data is affected, both Prototype I and Prototype II was tested. The device was sandwiched between the NIR test block and a temperature test rig, with 110g load applied to the FSR. The temperature test rig consists of a fan, heat sink, a Peltier element and a plate. The Peltier element has three settings: OFF(O), Hot(I) and Cold(II). A picture of the setup is presented in Figure 2.19. Cold settings cools the plate down to ∼8.5 degrees Celsius, while Hot heats the plate to ∼50 degrees Celsius.

The test was conducted over 50 minutes, with 10 minute interval between the different settings for the Peltier element: OFF, Hot, Cold, Hot, OFF.

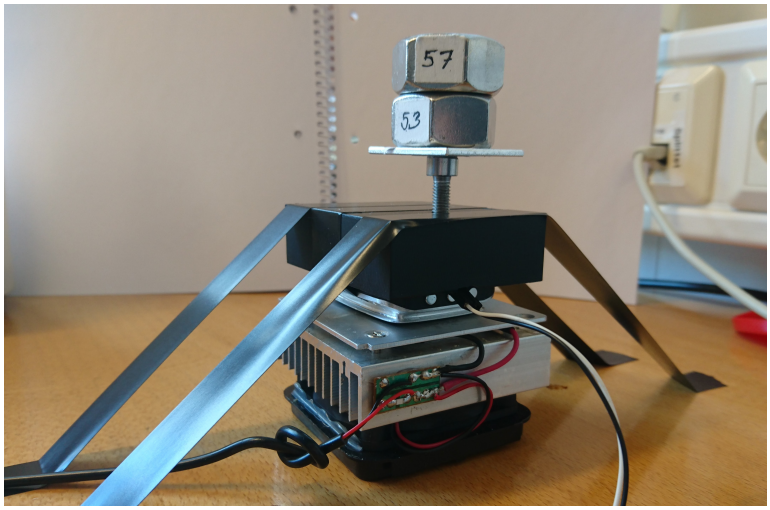

Figure 2.19: Setup for temperature testing

2.4.6 External force on the device

External forces acting on the BioMKR device may perturb the NIR data as a result of altering the tissue properties or by moving the device from its initial position. To see the effect of this movement artifact, the device is strapped to the subject's arm with strap tightness 1, and pressed by hand for a given duration.

At the beginning of the test, 1 minute is given for the measurements to stabilize before any external pressure is applied to the device. The test consists of the following steps:

1. External pressure is applied for 10 seconds
2. External pressure is removed for 10 seconds
3. Repeat the first two steps 3 times

These set of steps are repeated 3 times with 2 minutes rest in between sets. This is done for each adapter described in Section 2.1.7.

Chapter 3

Results

This chapter presents the results obtained by the tests described in the previous chapter. The data has been evaluated using MATLAB 2014a.

3.1 PCB bend test

Looking at Figure 3.1, the force clearly shows influence on the NIR signals. The results seem to be random in response to the force induced (increasing/decreasing NIR values), except for big enough forces, which consistently triggers a fall in NIR value.

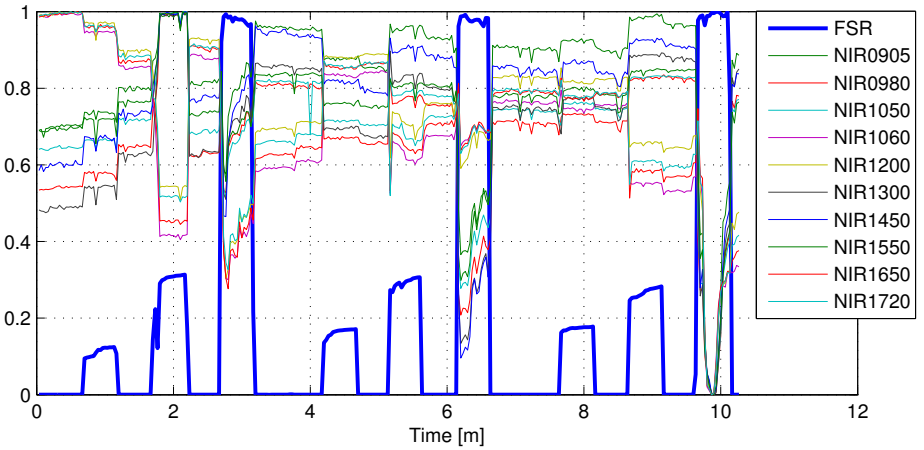

Figure 3.1: PCB bend test, Prototype II, normalized values

3.2 Strap test

Prototype I

As seen in Figure 3.2a, there is a stepwise increase/decrease in output voltage. The numbers correspond to the level of tension as defined in Section 2.4.3, and the procedure is repeated two times. Figure 3.2b shows a normalized plot on how the NIR data is affected.

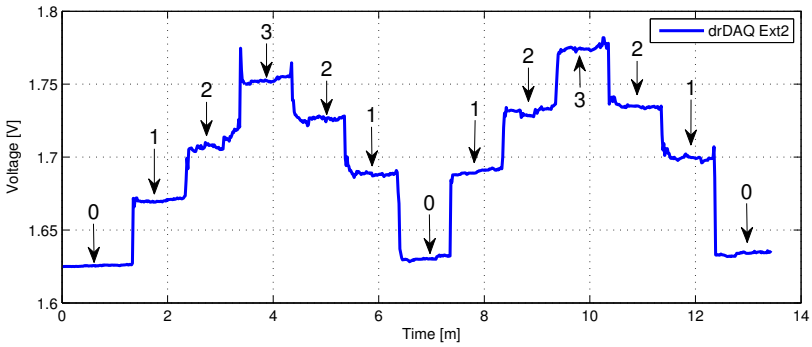

(a) FSR recorded with java

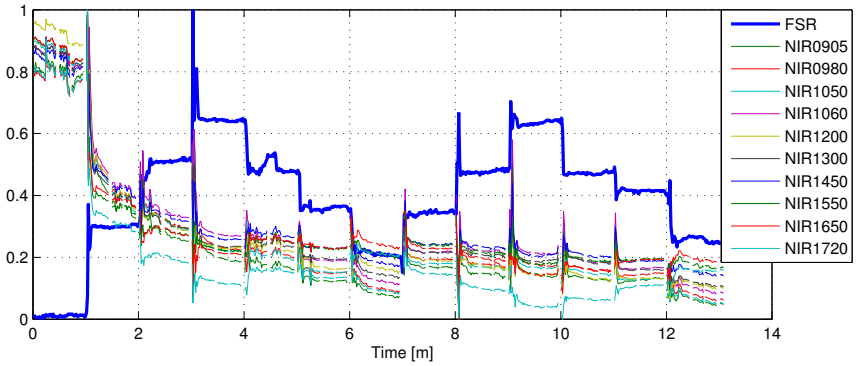

(b) NIR and FSR, normalized values

Figure 3.2: Strap test, Prototype I

Prototype II

The Prototype II device is suffering from little to no FSR actuation in the initial design. This section presents the results from the strap test using the different adapters described in Section 2.1.7. Figure 3.3a shows the normalized NIR response due to the strap tension changes where no adapter has been used to activate the FSR. Using Equation (3.1), we evaluate how much each wavelength changes from the initial NIR value (NIR_{start}), for three segments:

- after first cycle ($loose_1$-$light_1$-$tight_1$-max_1-$tight_2$-$light_2$-$loose_2$)
- from start to second instance of light tension ($light_2$)
- from start to end of experiment.

$$\frac{NIR_{new} - NIR_{start}}{NIR_{start}} \cdot 100\% \tag{3.1}$$

Tables 3.1 to 3.3 shows how mean change of all wavelengths for no adapter, Ø13T1.0FLAT adapter and Ø13T0.5CONE adapter. Standard deviation (st.d), as well as the wavelengths suffering the least and most change for the given segment is also listed. Tables and plots for the other adapters are listed in Section 6.2.

Segment	Mean (%)	st.d (%)	max (%)	min (%)
$Loose_1$-to-$Loose_2$	-6.55	-1.09	-8.09 (NIR0905)	-4.59 (NIR1300)
Loose-to-$Light_2$	-8.36	-1.56	-10.83 (NIR0905)	-6.10 (NIR1300)
Start-to-end	-8.97	-1.78	-11.34 (NIR0905)	-5.64 (NIR1300)

Table 3.1: Percent change in NIR signal value, no adapter

Segment	Mean (%)	st.d (%)	max (%)	min (%)
$Loose_1$-to-$Loose_2$	-8.25	-0.98	-10.58 (NIR1720)	-7.08 (NIR1200)
Loose-to-$Light_2$	-7.56	-0.83	-9.61 (NIR1720)	-6.61 (NIR1650)
Start-to-end	-10.45	-1.70	-14.14 (NIR1720)	-8.46 (NIR1060)

Table 3.2: Percent change in NIR signal value, Ø13T1.0FLAT adapter

Segment	Mean (%)	st.d (%)	max (%)	min (%)
$Loose_1$-to-$Loose_2$	-5.90	-0.85	-7.46 (NIR1720)	-4.46 (NIR1200)
Loose-to-$Light_2$	-4.72	-0.76	-6.30 (NIR1720)	-3.49 (NIR1200)
Start-to-end	-5.89	-1.22	-7.82 (NIR1720)	-3.80 (NIR1200)

Table 3.3: Percent change in NIR signal value, Ø13T0.5CONE adapter

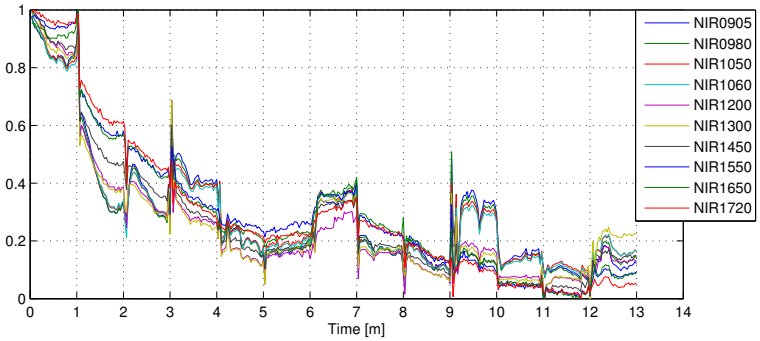

(a) No adapter. No FSR signal due to initial design, and is not included

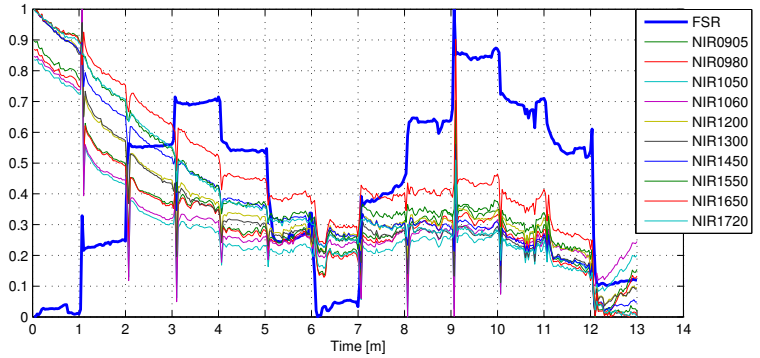

(b) Ø13T1.0FLAT

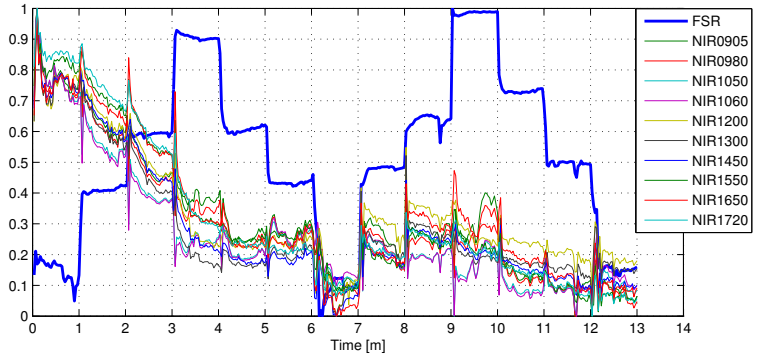

(c) Ø13T0.5CONE

Figure 3.3: Strap tests, normalized

3.3 Night test

Data collected during sleep with Prototype II attached to arm with strap tightness 1 will be presented here. Figure 3.4a shows how the data for short wavelengths may look like during the night. There are well defined spikes and several signal jumps in the data set, and although the FSR is actively logging, there is no actuation of the sensor due to the initial actuator design. The test is also conducted with the different test adapters, and the results for the handcrafted (Ø13T1.0TEST) adapter can be seen in Figure 3.4b. This is a typical response from the night tests, and it can be seen that the variations in the NIR signal coincides well with actuation of the FSR. Although NIR signals and FSR are coinciding, the increase/decrease in force does not consistently result in an increase/decrease in the NIR data.

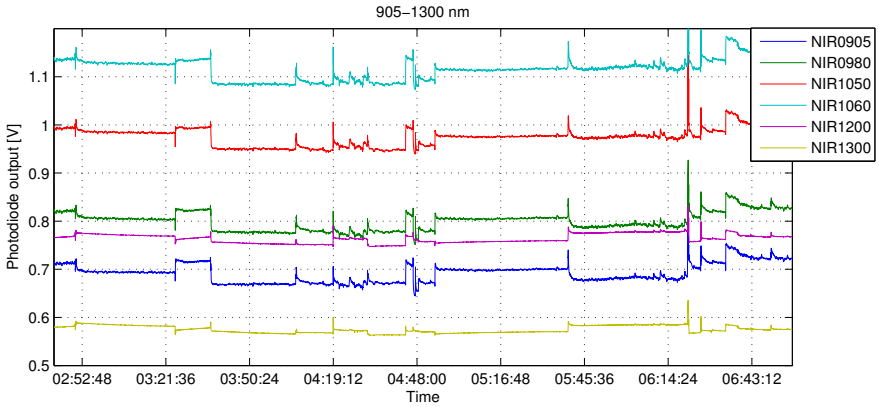

(a) Night test without adapter

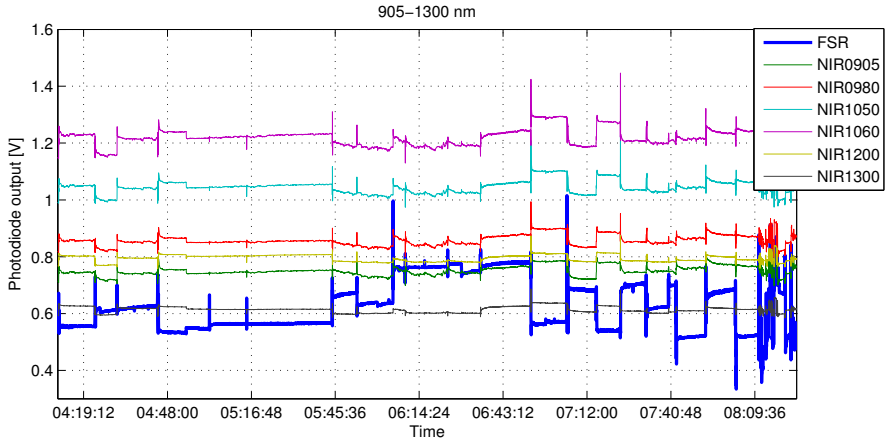

(b) Night test, Ø13T1.0TEST

Figure 3.4: Night Test with Prototype II

The accelerometer is often used as a motion artifact detector in various studies on eliminating the noise components in signals (Wood and Asada, 2006; Tong et al., 2002; De Luca et al., 2010). The BioMKR accelerometer is used to detect the number of acceleration events (defined as accelerations above 0.1G) that occurs during one measurement interval. The data collected during one of the night tests shows the importance of including another auxiliary sensor, such as the FSR, for motion detection. Figure 3.5 shows the data from (a) FSR, (b) NIR1300[1], and (c) accelerometer inside the BioMKR. It is seen that the accelerometer fail to pick up some of the more significant spikes in the NIR1300 signal (see arrows in Figure 3.5b). This is where the FSR excels as a motion artifact detector. Every clear signal change in the presented data set for the NIR1300 signal coincides with a signal change in the FSR.

[1]NIR1300 was selected as an example in this situation

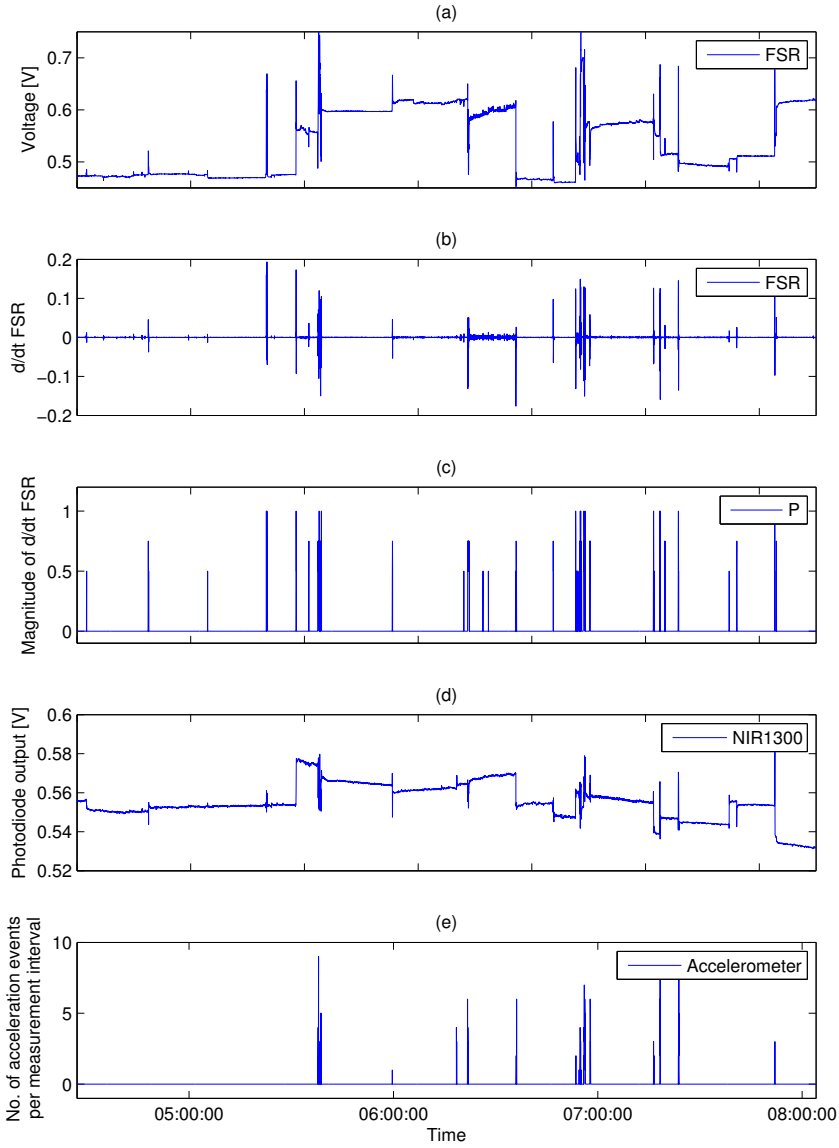

Figure 3.5: Night test, Ø13T0.5FLAT

The results from these night tests also depend on the amount of movement during the night, and possibly the amount of Rapid Eye Movement (REM) sleep cycles the given data set have captured before being overwritten. REM sleep is characterized by increased EEG activity, episodic bursts of rapid eye movement, as well as *muscle atonia*. The latter phenomenon refers to an almost complete paralysis of the body, as a result of motor neuron inhibition. Although random muscle twitching may occur (Carskadon and Dement, 2011). During the REM stage of the sleep tests, minimal movement artifacts from involuntary muscle movement could therefore be expected.

Figure 3.6 shows the indentation left in the skin with the different adapters. Clear differences is observed by looking at the thickness and shape between some of the adapters, e.g. Ø13T1.0TEST vs. Ø13T0.5CONE. The pictures are taken immediately after the device is taken off in the morning. Especially for the L30W4T1.0RECT adapter (Figure 3.6e), the indentation was quite significant, and the area felt itchy when taking the device off. The two adapters with thickness = 0.5mm was the ones that gave the least amount of indentation, which was expected (Figures 3.6b and 3.6d. The skin is also significantly less red and less irritated than the rest of the adapters.

(a) Ø13T1.0TEST

(b) Ø13T0.5CONE

(c) Ø08T1.0FLAT

(d) Ø13T0.5FLAT

(e) L30W4T1.0RECT

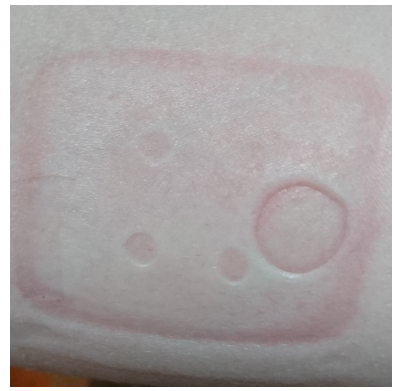

(f) Ø13T1.0FLAT

Figure 3.6: Indentation from the different adapters after night tests

3.4 Temperature testing

Prototype I

The temperature registered by the temperature sensor inside the Prototype I reached a peak of 40.9 °Celsius, and lowest value at 29.6 °Celsius. During the test, the FSR experienced an increase of 5.7% voltage, which corresponds to −8.79% resistance change. According to the datasheet (Interlink Electronics, 2013), -15% resistance change is to be expected for the FSR after 1hour at 85 °Celsius. But the FSR seemed unaffected by the switching of the temperature settings. As seen in Figure 3.7b, the NIR data is affected by the temperature variation. This is expected.

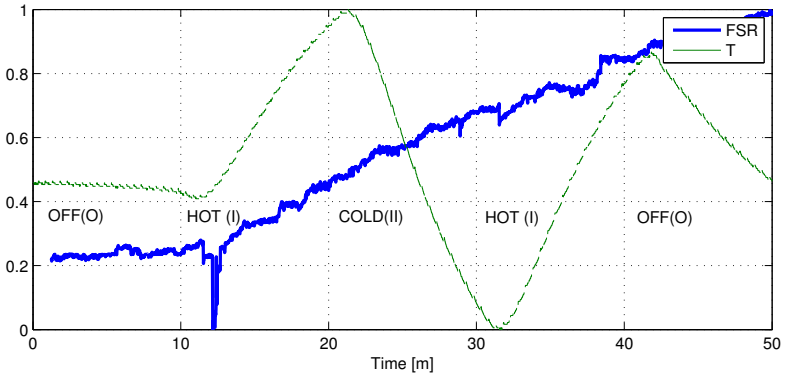

(a) Temperature and FSR data, normalized

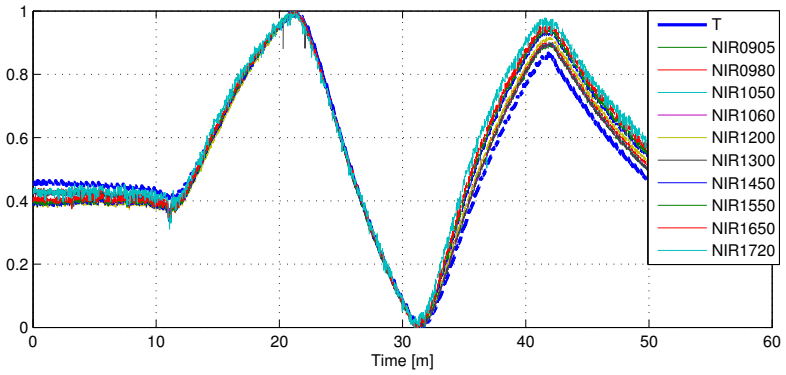

(b) Temperature and NIR data, normalized

Figure 3.7: Temperature testing Prototype I

Prototype II

The Prototype II has two separate temperature sensors mounted on each side of the PCB: T_{adc} and T_{device}. The T_{adc} sensor is located on the top side of the PCB, with the battery laying just above it, and is expected to be a little higher than T_{device}, which is located on the underside. This is observed for all tests included in this thesis.

The FSR drift is very similar as for Prototype I, but the NIR readings act very differently. This is a hardware difference from Rev.C and Rev.E, where the NIR is expected to have a negative correlation to temperature in Rev.E.

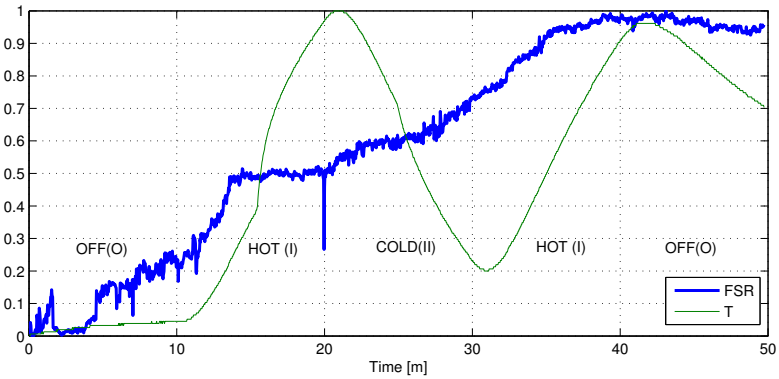

(a) Temperature and FSR data, normalized

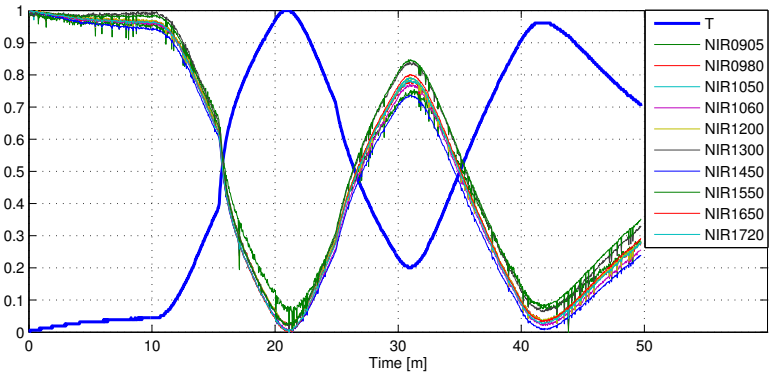

(b) Temperature and NIR data, normalized

Figure 3.8: Temperature testing Prototype II

The temperature test was repeated, as the FSR data seem unaffected by the temperature switch which clearly was present in Nøstbakken (2016). The results are now completely different, where the FSR has a negative correlation with the temperature development. The spikes seen for the FSR (e.g. at 20 minute mark) may be a result of unstable test setup, since the temperature switching is done with a mechanical toggle. The signal swing for both the OFF (0) phases in Figure 3.9 may be correlated with a battery charge cycle, increasing the temperature inside the device by ∼2.3 and 2.6 °Celsius, respectively.

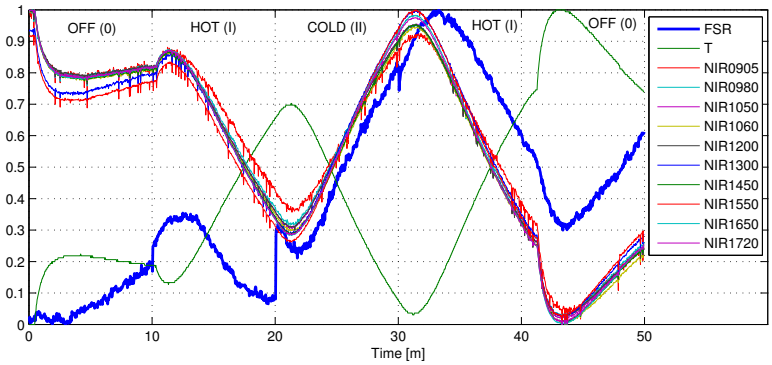

Figure 3.9: Second temperature test of Prototype II, normalized values

The most significant change that the FSR exhibits, is about 3 minutes after the cold session is done (see Figure 3.10). The peak value is 2.87% higher than the initial value was when the test started. The signal drift in the beginning is almost negligible, 0.51%.

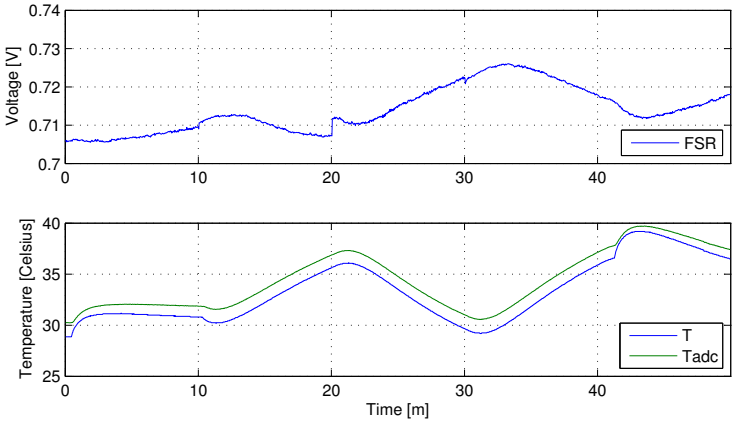

Figure 3.10: FSR response to temperature change. Comparison of T_{adc} and T_{device}

3.5 External force

The data from the test described in Section 2.4.6 has been divided into four sections corresponding to the time where no external force was applied (see Figure 3.12). The mean value for each wavelength for the given segment is calculated, and the percent change between segments is presented in tables and figures.

Prototype I

As can be seen in Table 6.8 and fig. 3.12, the NIR signal does not suffer very much change from section to section. The data responds to the forces induced, but settles back again to approximately the same level as before.

Table 6.8 shows the mean percent change for each wavelength in Prototype I.

	Mean (%)			
Wavelength	Segment 1-2	Segment 2-3	Segment 3-4	Segment 1-4, Total
NIR0905	-0.54	-0.79	-0.69	-2.01
NIR0980	-0.34	-0.95	-0.74	-2.02
NIR1050	0.30	-0.76	-0.44	-0.90
NIR1060	0.33	-0.66	-0.20	-0.53
NIR1200	0.74	-0.37	0.13	0.50
NIR1300	0.51	-0.47	-0.12	-0.08
NIR1450	0.10	-0.72	-0.25	-0.87
NIR1550	1.30	-0.04	0.05	1.31
NIR1650	0.61	-0.35	0.01	0.28
NIR1720	-0.49	-1.14	-0.36	-1.98

Table 3.4: Mean percent change in NIR signal value for Prototype I

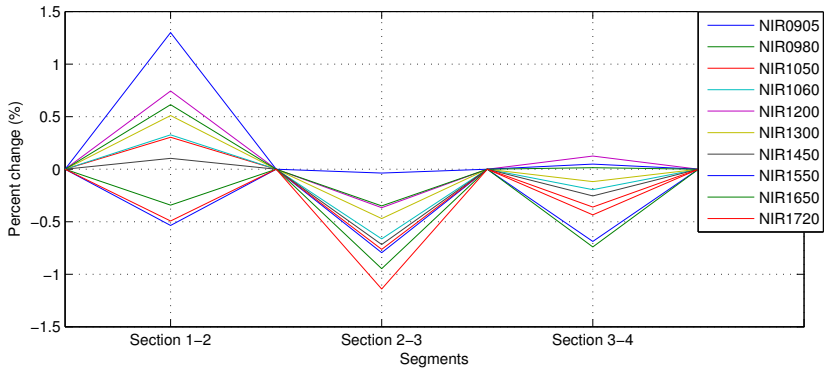

Figure 3.11: Percent change in NIR values from section-to-section

For most of the cases, the section-to-section changes are less than ±1%. As seen in Table 6.8, *NIR1550* is the signal that exhibits the most signal change after the first segment, while *NIR0905*, *NIR0980* and *NIR1720* is suffering the most overall change. Figure 3.11 gives a visual representation of the variation in the NIR data between the three segments.

Typical FSR response, as well as *NIR1550* is seen in Figure 3.12. Due to how the Prototype I logs the BioMKR data, the plotted line for *NIR1550* in appears dotted due to missing values.

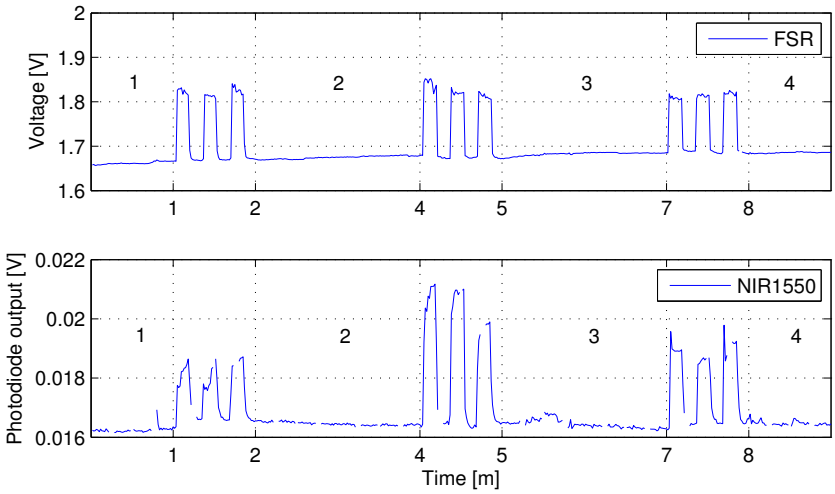

Figure 3.12: Prototype I, NIR1550 output as a response to the force.

Prototype II

When the Prototype II device was subjected to external force, the NIR data experienced a distinct spike for the duration of applied force. After each sections of press/release actions, the general observed response in NIR is settled at a lower value than before the force was applied (i.e. λ=1550nm, Figure 3.13b). This happens both with and without any adapter, and some of the wavelengths will continue to decrease in between sets (i.e. λ=1720nm, Figure 3.13c). The continued decrease in NIR values is observed for wavelengths from 1200nm to 1720nm. This is most likely a temperature effect as a result of an un-standardized BioMKR device.

	Mean (%)			
Wavelength	Segment 1-2	Segment 2-3	Segment 3-4	Segment 1-4, Total
NIR0905	-6.23	-1.40	-0.28	-7.80
NIR0980	-5.29	-1.37	-0.54	-7.09
NIR1050	-4.09	-1.09	-0.84	-5.93
NIR1060	-4.23	-0.86	-1.09	-6.10
NIR1200	-3.06	-0.88	-1.08	-4.95
NIR1300	-2.11	-0.71	-0.59	-3.37
NIR1450	-5.54	-1.38	-0.31	-7.14
NIR1550	-4.99	-1.45	-0.57	-6.90
NIR1650	-3.99	-1.18	-0.92	-6.00
NIR1720	-4.17	-1.11	-1.22	-6.39

Table 3.5: Mean percent change in NIR values from section-to-section, Prototype II, no adapter

As we can see from Table 3.5, the NIR signals suffers 2-7% drop after the first segment, even without an adapter. This is a considerably larger change than what is observed in Prototype I. This is also observed for the different adapters, which will be presented in Figure 3.14. The tables for each plot can be found in Section 6.2.

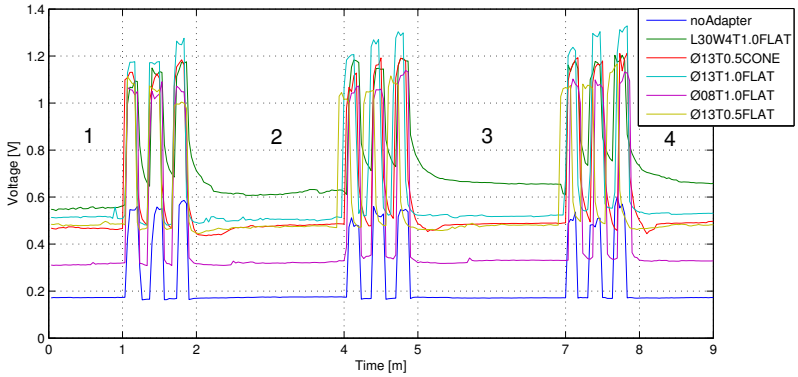

(a) FSR

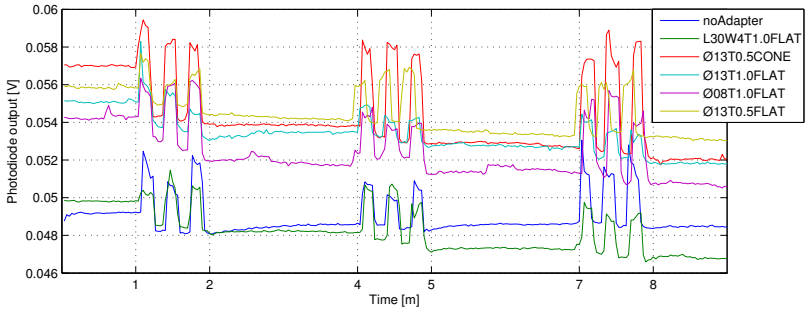

(b) NIR1550, example of stable resting

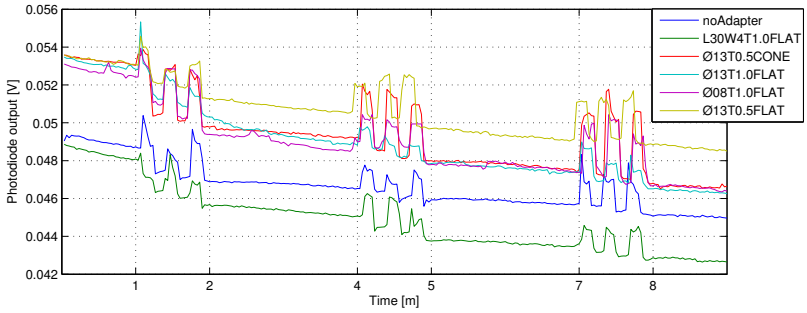

(c) NIR1720, example of decreasing resting

Figure 3.13: Response to external forces

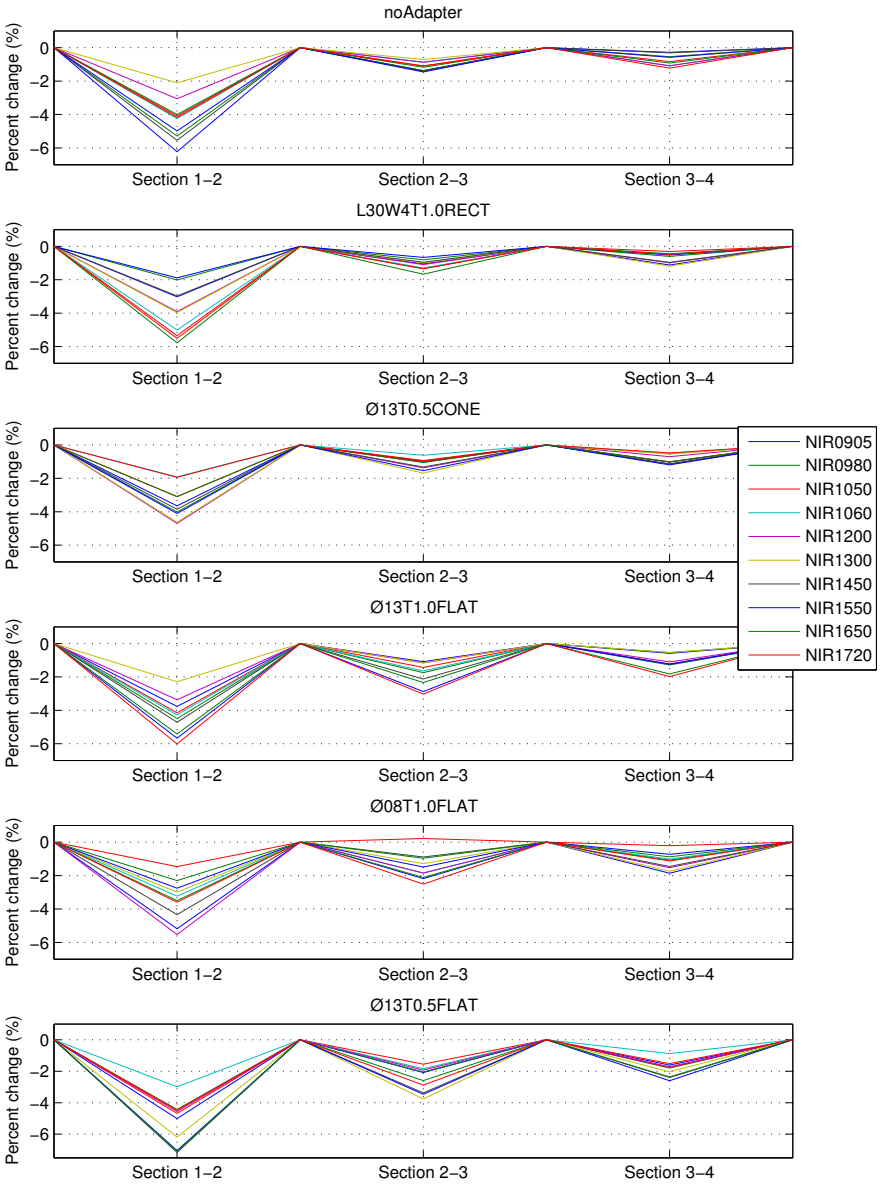

Figure 3.14: Percent change in NIR values, Prototype II, all adapters

Chapter 4

Discussion

4.1 Strap tightness and tissue properties

As stated in Section 1.4.2, a number of studies report alteration of the tissue properties when subjected to external forces, which again can affect the NIR diffuse reflectance. As can be seen in Figures 3.2b and 3.3, there is a distinct drop in NIR signals when the strap is tightened from grade 0 (loose_1) to grade 1 (light_1). This also happens the first time external forces are induced on the device during the 'External Force' test described in Section 2.4.6. According to Chen et al. (2005), this can be explained by an increase in absorption coefficient(μ_a) and reduced scattering coefficient(μ_s') as the result of increasing compression of the skin, thereby reducing the reflectance. The same is observed in Chan et al. (1996), where the increase in absorption coefficient was explained by alteration of the blood volume in the area under *slight* compression, which can significantly modify μ_a. The increase in volumetric water concentration due to tissue thickness reduction is also suggested to be a possible contributor to increasing absorption, especially for longer wavelengths, where light is strongly absorbed by water (Cugmas et al., 2014).

Shangguan et al. (1998) reported irreversible tissue properties if the structure cannot recover after compression. This was investigated through strap tests, where the adapter was changed without taking the Prototype II off. Figure 4.1 shows how the first (*Ø8T1.0FLAT*) and third (*Ø13T0.5FLAT-TissueRecover*) curves starts with a higher NIR value and suffers a distinct downward slope in photodiode output for the first 4-6 minutes of the test. The second curve (*Ø13T0.5FLAT*) has not the same tendencies. This suggests that the tissue has not fully recovered after the first test with *Ø08T1.0FLAT*, similar to what was discovered by Shangguan et al. (1998). Although, the reflectance is somewhat higher than where *Ø8T1.0FLAT* left off. This might be a result of lifting up one side of the Prototype II to change the adapter, giving some tissue more chance to recover to a certain degree. The second test was conducted within 4 minutes after the previous run, while *Ø13T0.5FLAT-TissueRecover* was done almost two hours later.

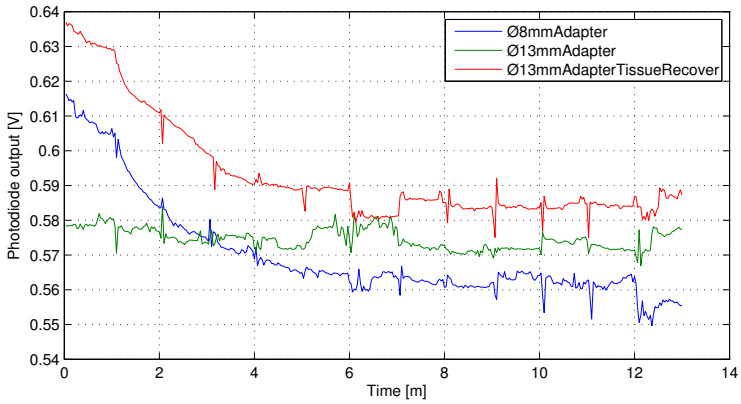

Figure 4.1: Effects of tissure recover

4.2 Consequence of FSR placement

An important factor to evaluate with the current setup, is how the NIR values will be affected by the sensor placement, and if it will contribute in perturbing the NIR signal. By placing the FSR with its back being supported by an IC on the PCB, all forces must be taken by the PCB itself or the holding points for the PCB (i.e. the screws). As presented in Section 3.1, it is clearly shown that NIR signals change when subjecting the PCB with force (see Figure 3.1). Since there is no tissue involved in these tests, the change behind the NIR signals may be due to the PCB flexing. This is a consequence of placing the FSR directly on the PCB without any mechanical restrengthening of the PCB. Although, this test was conducted with a very direct force and of larger magnitude than to be expected when worn on the arm, which is presented in Section 3.2. In the strap tests, the change in NIR signals are not as drastic and have more monotonic tendencies (see e.g. Figures 3.2b, 3.3a and 6.4). A big difference between the PCB bend test and strap tests, is that the NIR resets itself to a certain degree in the PCB bend test. This may be because there is no tissue being compressed, and therefore no alteration in the measured site. The pit in the measurement rig which the BioMKR is measuring does not change between increase/decrease of force. Although, the NIR settles at different levels between the cycles. The PCB may have been moved slightly out of place, or not resettled itself after bending, which again can shift the LEDs and/or photodiode. The entire device may also have moved as a result of the forces, since the test block is not a perfect fit for the BioMKR.

As can be seen in the tests conducted during sleep(Section 3.3), the NIR signal is affected by sudden and significant changes, regardless if there is an actuator adapter or not. But the adapter may also contribute to larger NIR signal variations depending on the degree in which the adapter pushes down on the FSR and PCB. In six out of ten NIR spectra, the signal drops more when the Ø13T1.0TEST adapter is used in the strap tests as opposed to no adapter at all (see Figures 6.2 and 6.3 in Section 6.2). It is seen by the results that placing the FSR directly on the PCB may be perturbing the NIR signals even more.

Both Rev.C and Rev.E BioMKR devices was expected to have temperature dependencies, which was also confirmed for both prototypes in Section 3.4. But the FSR seemed surprisingly unaffected by the temperature changes, as opposed to the findings in Nøstbakken (2016). When doing a second test with Prototype II, the results changed significantly (see Figure 3.9). Here the FSR is changing its output according to increasing or decreasing device temperature. It is curious how these results can differ so much in an identical test procedure. The second test was conducted after some mechanical issues regarding screw holding points for the device circuitry had been fixed, by re-threading and replacing the initial screws. A consequence of this process was the FSR now gives a signal corresponding to $\sim$150mV for unloaded situations, as opposed to the previous zero signal, i.e. the PCB may be under additional stress.

It is believed that the mechanical expansion of materials may also change the signal output. As the temperatures increase, the kinetic energy of the materials' molecules increase, leading to molecule vibration/movement. This leads to an

expansion in the material, and could ultimately alter the properties of the FSR and/or surrounding materials. Kühl (1999) investigates how PCB's and thick film chip resistors are affected by both temperature cycles and mechanical stress. Their findings suggests that there can be significant resistance changes due to PCB bending and temperature changes. With the FSR measurement circuit being positioned directly behind the device glass that is in contact with the temperature test rig, the components here may suffer changes due to the temperature development. The temperatures the components has been subjected to in Kühl (1999) are of greater magnitude than presented in this study, but it may be part of the explanation towards the significant result changes.

As for the changes regarding the components' resistance on a bent PCB, subjecting the BioMKR PCB to forces that can cause bend is reported to have a piezoresistive effect to thick film components, which may lead to overall performance differences of the device.

4.3 NIR change in Prototype II for external force testing

There is a big difference in how the NIR signal is affected by pressing on the device for Prototype II compared to Prototype I. As presented in Section 3.5, NIR signals in Prototype I are both increasing and decreasing, while Prototype II consistently suffers a reduced NIR signal after the push/release actions. This may be a result of the mechanical differences between the two prototypes. The external force test was conducted after the screw holes had been modified to fit new set of screws for Prototype II. If these mechanical differences enables more movement or permanent misalignment of the PCB, it may be the reason for the observed variation. Figure 4.2 shows how the NIR data is affected for the different adapters.

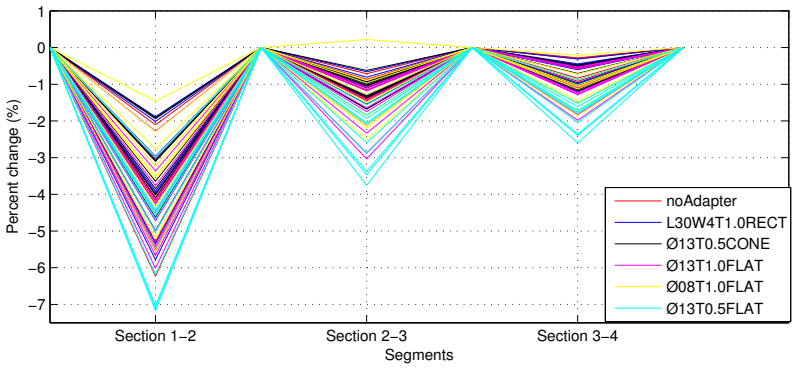

Figure 4.2: NIR signal change for all adapters, Prototype II

4.4 PLS regression of NIR/FSR data

Partial least squares regression (PLSR) is a statistical method used to find relations between two data sets, X and Y, by finding linear independent combinations of X that explains most of the variance in Y. We tried using PLSR with column centering and cross validation to model the FSR signal (Y) using the 10 NIR spectra (X) from the night experiments. We used 4 segments with block sequence for cross validation. This means that data set is divided into 4 equally large contiguous segments, and the PLSR builds a model of the FSR signal for the first three segments, and tests how well the model performs on the fourth segment. The PLSR modeling was done using Prediktor's software, and the results was imported for plotting in MATLAB 2014a.

Figures 4.5 and 4.6 shows how well the model performs in recreating the FSR signal, using the component with the lowest standard error of validation (SEV), as presented in Table 4.1. The predicted curve is not successfully mimicking the complete behavior of the reference FSR curve in either of the plots. At most, we are able to capture 79% of the variance in the reference data, and there are sections where the predicted curve struggles to come close to the actual reference (Figure 4.6b). The number of components used to model the behaviour is quite high, though.

Adapter	Test	No. rows	Explained variance in Y	Component with lowest SEV	SEV
Ø13T0.5CONE	Night Test	7334	67%	9	0.049
Ø13T0.5FLAT	Night Test	6940	75%	10	0.056
Ø13T1.0FLAT	Night Test	6511	79%	10	0.034
Ø08T1.0FLAT	Night Test	6500	75%	10	0.040
L30W4T1.0RECT	Night Test	6646	65%	5	0.053

Table 4.1: PLS regression

Although, these test results are biased by the period under evaluation. Since the flash memory in Prototype II is of finite size, we are not able to capture FSR data from the entire night. As a preemptive measure to get a more accurate PLSR model of the night tests, the last data points recorded before powering off the device has been cut out of the data set. These last minutes produce highly variating FSR and NIR data due to e.g. fiddling with the device strap (see Figure 3.4b). These data points are not considered to be of any relevance to the night test.

The regression coefficient for the PLSR models are given in Figure 4.3 (Table 6.9 in appendix). The coefficients state the contribution each of the NIR spectra has towards predicting the FSR signal. Too much variation in the coefficients between the different models suggests that the correlation between the NIR signal and FSR signal is weak. Looking at Figure 4.3, NIR1050 is the most consistent signal in the predictions, but the overall observation suggests that there is too much variation in the regression coefficients.

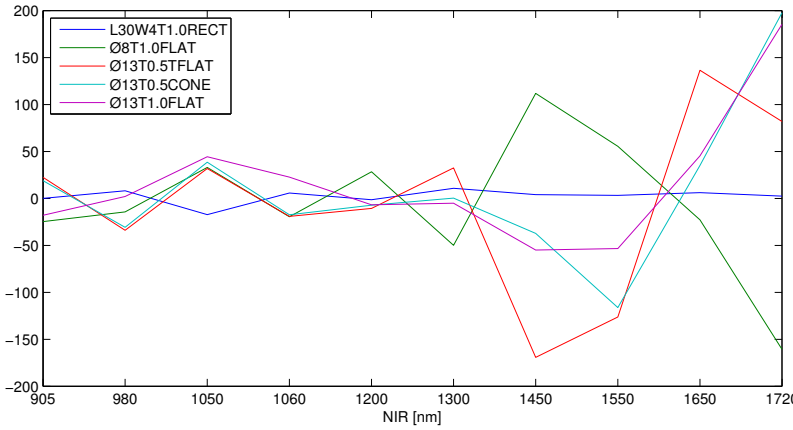

Figure 4.3: Regression coefficients

4.4.1 Building model from data set A and predict FSR in data set B

Another way to check if the NIR signals and FSR signal are correlated is by building a PLSR model of a given data set, and try to predict the FSR values in a different data set. The regression coefficients from Figure 4.3 imply that the correlation is too weak to produce satisfactory results. Two models from the night tests have been built: Ø13T1.0FLAT and Ø08T1.0FLAT. These models (A) are used to predict the FSR signal in the other night tests (B) based on the NIR data in data set B. Looking at the scatter plot in Figure 4.4, the clustered result indicate that there is not a clear linear relationship between the predicted FSR signal and the original FSR signal. Ideally, these plots should have formed a straight line corresponding to X = Y. Figures 6.8 and 6.9 shows the performance when the model tries to reproduce the night tests.

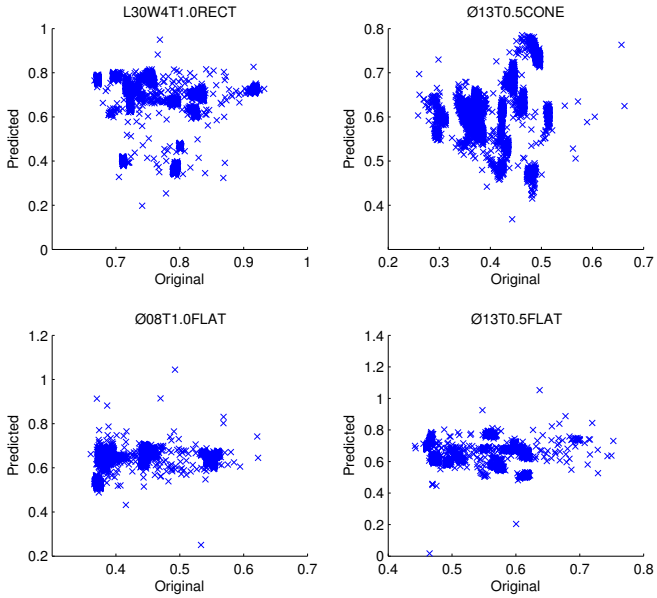

(a) Predictions with model built from Ø13T1.0FLAT night test

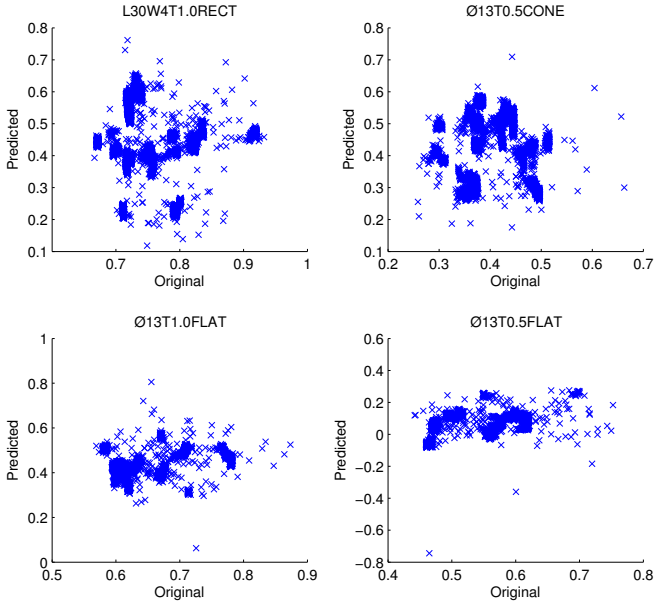

(b) Predictions with model built from Ø08T1.0FLAT night test

Figure 4.4: Predictions made by data set A to fit FSR response in data set B

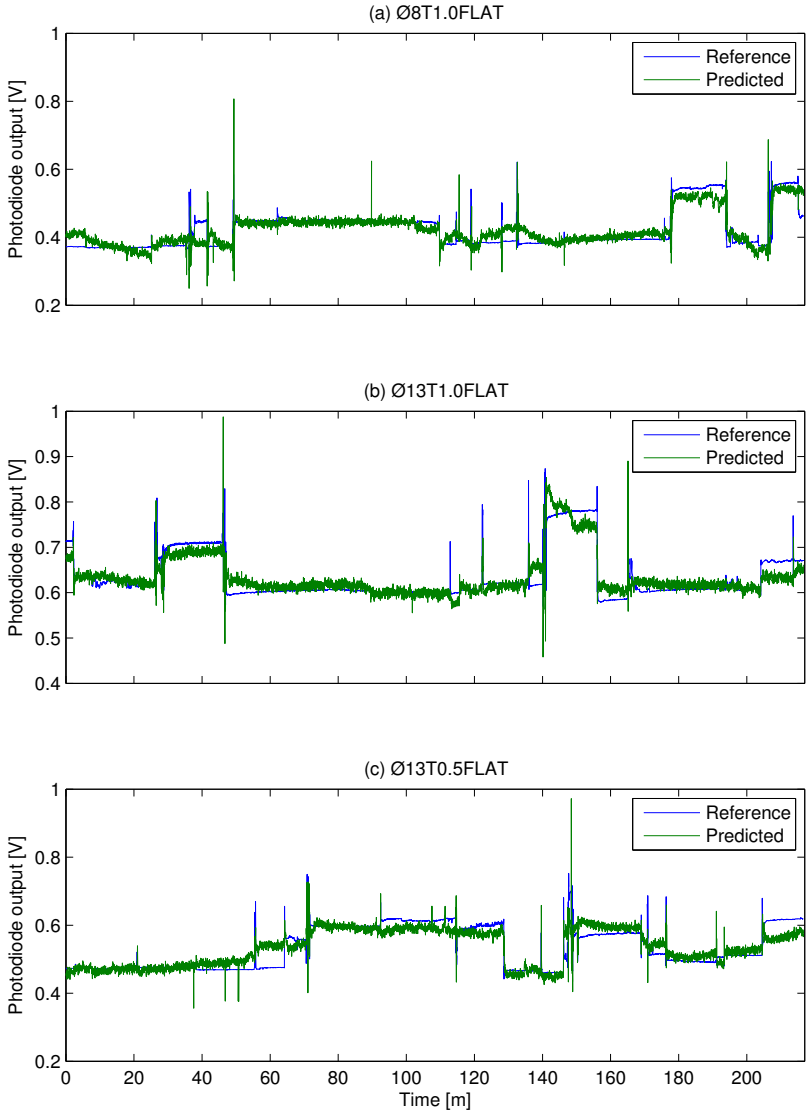

Figure 4.5: Predicted FSR with PLSR

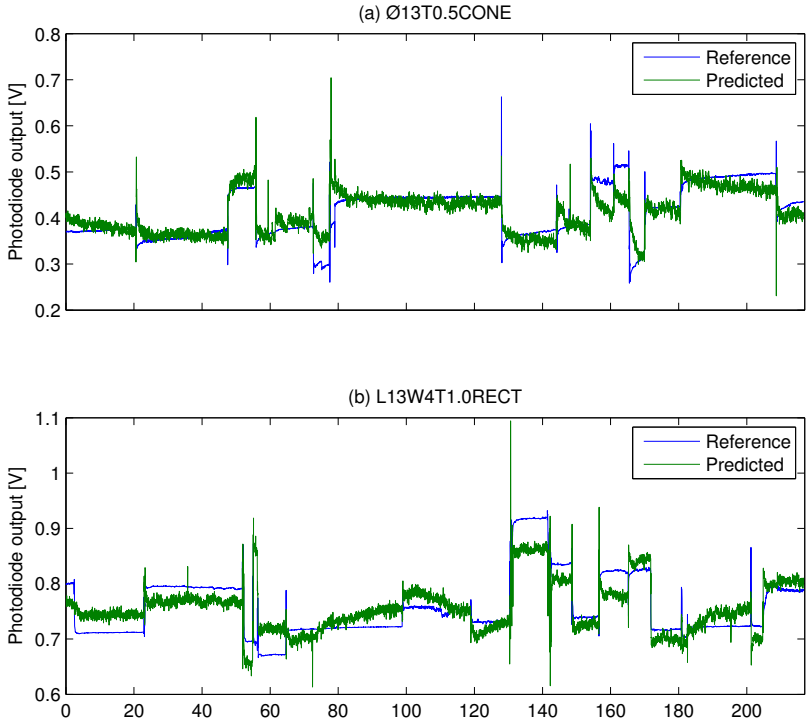

Figure 4.6: Predicted FSR with PLSR

4.5 Adapter performance

When it comes to the different adapters tested, there is no adapter that stands particularly out as the best option. Considering indentation left in the skin after night testing, the adapters with smallest thickness (T=0.5mm) outperformed the others. The Ø13T0.5CONE gave a slightly more clear edge than Ø13T0.5FLAT, due to its thin and sharp edges. All the others left a red and itchy skin, where the L30W4T1.0RECT was the most uncomfortable. The FSR signal strength and the ability to detect NIR jumps during the night proved satisfactory for all adapters. Different sleep cycle and activities are also factors that may come in to play with respect to night test results. FSR signal strength, PCB bending, tissue compression as well as adapter indentation all depends on the combination of the geometric shape of the adapter and involuntary movement during sleep. For adapters yielding strong marks in the skin, subject may have been asleep on top of the device the last X hours, making a more significant indentation, and not necessarily just the shape of the adapter. This will produce a higher output from the FSR.

None of the adapters affected the NIR Dark parameter.

The results from the external force test with Prototype II showed that the NIR suffered the greatest signal change after the first set of push/release actions. With up to 7% signal reduction, and further ∼1% decrease for each of the two next segments. The test conducted with Ø13T0.5CONE gave the overall smallest change, where none of the wavelengths suffered more than 7% signal drop, and a mean reduction of 5.44% (see Table 6.5). In comparison, the run without adapter suffered a mean drop of 6.17% with three wavelengths above 7% reduction. This might indicate that the adapters for this test was not the main contributor for NIR signal perturbation. The act of pushing the device against the arm was done by hand, and could have been done with different magnitude and/or direction each time. This could lead to the variation between the data sets.

Evaluating the response from the strap tests, the coefficient of variation is calculated for each of the 13 segments of the test (see Table 4.2), where 0 indicate *Loose* strap tension, and 3 indicate *Max* strap tension. On average, Ø13T1.0FLAT is the adapter that shows the most stable response. This can also be seen in Figure 4.7. The two other adapters with a diameter Ø=13mm also performs very well to the strap test.

Because of mechanical difficulties, creating adapters with 0.5mm thickness proved troublesome when using plastic material. There was scheduled to make a Ø08T0.5FLAT adapter, but the creation of this resulted in its edges being folded outward like a cup. In other words, the edges would dig into the skin when used with the device. This was most likely due to the heat from the machinery making it.

As well as scoring the highest in explained variance from PLSR modeling, Ø13T1.0FLAT or Ø13T0.5FLAT are good candidates for how the finalized adapter should look like. The overall performance indicate that the adapter should be a round adapter with a thickness between 0.5mm and 1mm.

	Coefficient of Variation (%)					
Tension	Ø13T1.0 TEST	L30W4T1.0 RECT	Ø08T1.0 FLAT	Ø13T0.5 FLAT	Ø13T0.5 CONE	Ø13T1.0 FLAT
0	49.36	0.28	1.35	2.59	3.77	1.48
1	2.72	19.48	1.44	0.79	0.59	0.99
2	6.08	8.66	0.47	0.76	0.49	0.17
3	0.95	4.07	1.92	2.69	0.53	0.33
2	1.03	5.21	2.24	0.38	0.66	0.55
1	1.49	7.23	0.28	0.50	0.40	1.16
0	90.62	0.29	0.61	5.22	6.93	2.81
1	3.60	0.31	3.91	1.15	0.69	1.84
2	3.07	7.08	1.30	0.18	1.85	1.11
3	0.72	4.73	0.48	0.44	0.30	0.49
2	1.16	1.21	2.21	0.42	0.23	1.93
1	1.37	7.41	0.21	0.42	1.40	1.43
0	10.92	0.27	2.82	1.29	1.93	0.87
Average	13.31	5.09	1.48	1.29	1.52	1.17

Table 4.2: Coefficient of variation from strap testing (% CV)

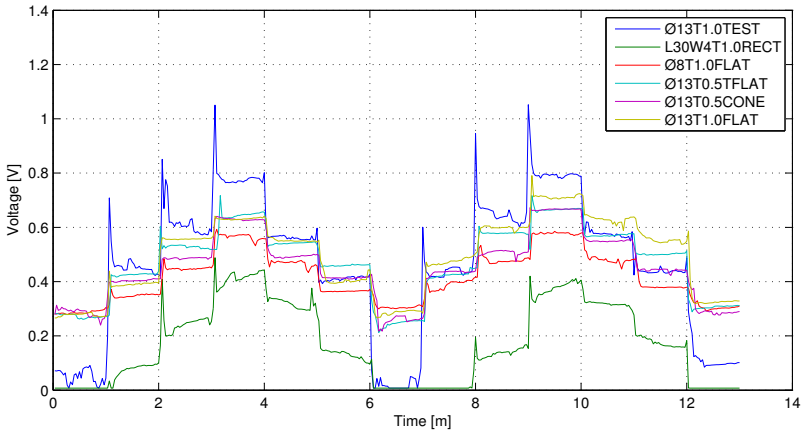

Figure 4.7: Strap test FSR response with different adapters

4.6 Use of FSR data for signal correction

As presented in Section 3.3, the events where NIR signals significantly perturbed, the FSR also exhibited a more distinct change than regular drift. The timestamps coincide with each NIR measurement, and it may be a good indicator for when body movements or muscle movements occur during sleep. As PLSR performance indicate, the characterization of how the forces affect the NIR signals is not clear. Looking at the results presented in Figure 3.5, it is obvious that with the help of the FSR data, we are able to capture more of the motion artifacts corrupting the NIR readings, compared to accelerometer detections alone.

Examining a given FSR data set, we can set up conditions for how severe the signal changes must be to be regarded as significant. An example of this is Figure 4.8c, where P indicate the magnitude of $\frac{d}{dt}FSR$ according to Listing 4.1.

Listing 4.1: Caracterization of $\frac{d}{dt}FSR$

```
dy1 = diff(FSR)./diff(time)

for i=1:lenght(dy1)
    if((abs(dy1(i))>0.01)&&(abs(dy1(i)<0.02)))
            dyC(i) = 0.5;
        elseif(abs(dy1(i)>0.02)&&(abs(dy1(i)<0.1)))
                dyC(i) = 0.75;
        elseif(abs(dy1(i)>0.1))
                dyC(i) = 1;
        else
            dyC(i) = 0;
    end
end
```

As previously stated, the accelerometer capture fast changes in velocity, and thus unable to register slow developing artifacts such as an increasing force acting on the PCB. By modeling the FSR data in the same manner as the accelerometer data, we are able to capture much more of the changes seen in NIR1300 data. Figure 4.8 shows how 'P' and 'Accelerometer' together capture every significant changes in 'NIR1300'.

The BioMKR already uses the accelerometer and parameters such as the NIR Dark to determine if the NIR signals can be trusted to represent the correct estimates of reflectance. The FSR can now function as an additional auxiliary sensor for this trust calculation. This can be the first step towards handling the motion artifacts that corrupts the NIR signals. This has only been tested with previously recorded data set, and not real time while logging. This should be further investigated, and this data could be used in the same manner as Choi et al. (2007) as an coefficient update blocker for adaptive filtering methods. As previously mentioned, Wood and Asada (2006) used Widrow's Active Noise Cancellation algorithm in PPG measurements for motion artifact removal. Similar to the measurements done in BioMKR, the PPG measurement system consists of an LED array with corre-

sponding photodiode. Due to the similarities, the use of Widrow's ANC algorithm in BioMKR should be investigated.

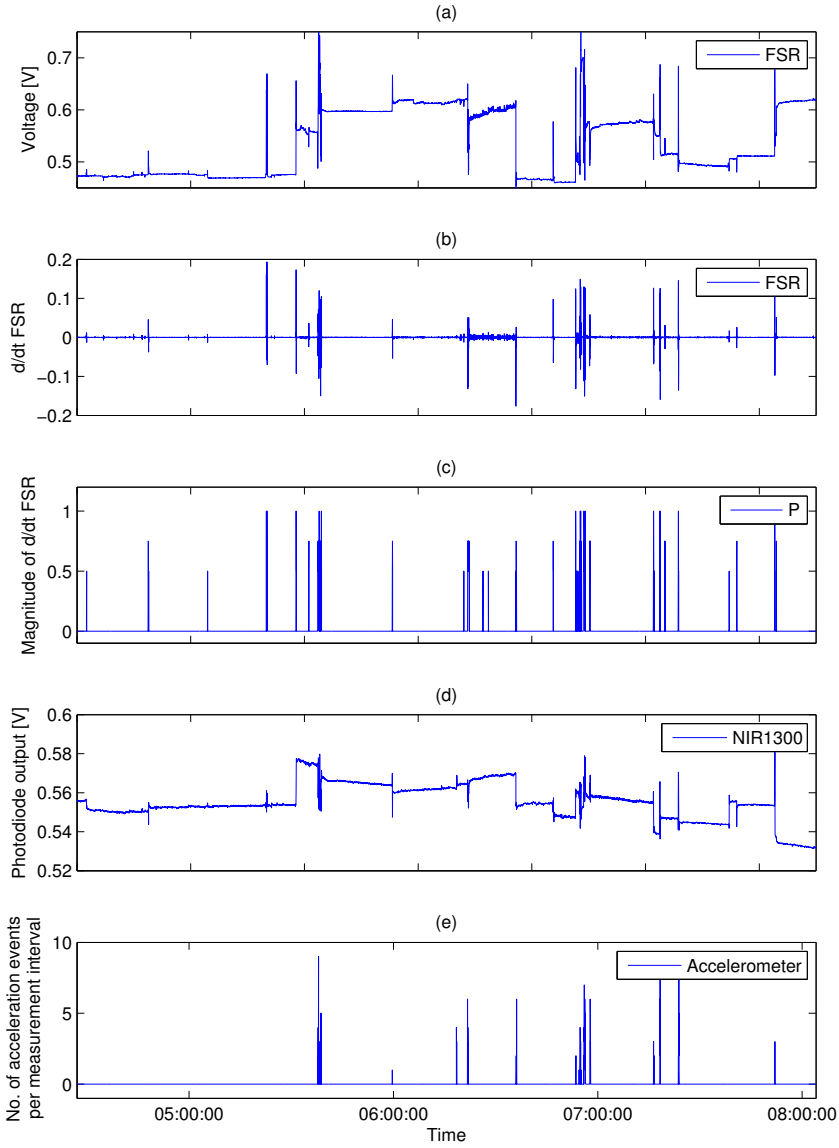

Figure 4.8: Event marker for rapid force changes

Chapter 5

Conclusion

The influence of motion artifacts in the BioMKR data limits the accuracy of correct glucose estimates. The investigation on how external force and pressure affects the measurements have been done with the use of a single FSR sensor. The sensor has been implemented with a fully functional BioMKR device, and the NIR data of tissue in the anterior upper arm has been under evaluation.

It is seen that the NIR signals read by the BioMKR change when the device is exposed to external pressure. The FSR sensor is able to capture most of these events when an appropriate adapter is used, and successfully registers every significant NIR change from involuntary movement during sleep. PLSR method is used to investigate the correlation between the measured NIR signal and forces picked up by the FSR, but there was not discovered a solid correlation in the data sets. It is believed that the tissue undergoing structural changes as a result of the external pressure affects the NIR signal in a way that the force sensor alone is not able to predict.

It is seen from experiments that the placement of the FSR directly on the PCB is perturbing the NIR signal, and should not be considered unless there is any mechanical restrengthening of the circuitry. The performance of the chosen FSR sensor is proven to give satisfactory results, and could be an appropriate sensor in the finalized design. It is proven to register the external forces that is subjected to the prototypes during testing, which coincides well with timings of significant NIR variations.

From this study, the interface between the skin and the FSR sensor that provided the best results concerning signal stability and skin indentation was adapters with a circular shape with diameter Ø=13mm and thickness T=0.5-1.0mm. The thicker the adapter, the more clear indentation to the skin. Sharp edges should also be avoided for adapter design.

5.1 Suggestions for future work

The force sensor should be placed differently, preferably where minimal contact between BioMKR circuitry can be achieved. The FSRs used in this work are quite slim, and a socket with strong enough back support could be milled in the casing bottom, with the appropriate actuation from underside of the device. The feasibility of this should be investigated.

The data generated from the FSR should be tested in an adaptive filter approach, as the literature study presents successfully results with this method.

The FSR sensor should be calibrated to force (N) or pressure (Pa) as opposed to the current voltage output. This will give a more intuitive measure on FSR signal, and should be done once the final integration design has been developed. This is to ensure correct signal when all the mechanical dependencies are known (e.g. proper back support, amount of active sensor area actuated, size of the interface towards the skin etc.).

Temperature dependency should be further investigated, both for the FSR signal as well as for the BioMKR data.

An in depth investigation on how the tissue optical properties change as a response to external forces should be conducted. Although there are several studies showing inconsistencies in reported results, a study with BioMKR specifics should be done.

Bibliography

Amphenol. *NovaSensor NPC-410 Series*, August 2014. Data sheet.

A N Bashkatov, E A Genina, V I Kochubey, and V V Tuchin. Optical properties of human skin, subcutaneous and mucous tissues in the wavelength range from 400 to 2000nm. *Journal of Physics D: Applied Physics*, 38(15):2543, 2005. URL `http://stacks.iop.org/0022-3727/38/i=15/a=004`.

Jeffrey A. Bluestone, Kevan Herold, and George Eisenbarth. Genetics, pathogenesis and clinical interventions in type[thinsp]1 diabetes. *Nature*, 464(7293):1293–1300, 2010. ISSN 0028-0836. doi: http://www.nature.com/nature/journal/v464/n7293/suppinfo/nature08933_S1.html.

Mary A. Carskadon and William C. Dement. Chapter 2 - normal human sleep: An overview. In Meir H. Kryger, Thomas Roth, and William C. Dement, editors, *Principles and Practice of Sleep Medicine (Fifth Edition)*, pages 16 – 26. W.B. Saunders, Philadelphia, fifth edition edition, 2011. ISBN 978-1-4160-6645-3.

E. K. Chan, B. Sorg, D. Protsenko, M. O'Neil, M. Motamedi, and A. J. Welch. Effects of compression on soft tissue optical properties. *IEEE Journal of Selected Topics in Quantum Electronics*, 2(4):943–950, Dec 1996. ISSN 1077-260X. doi: 10.1109/2944.577320.

Wenliang Chen, Rong Liu, Kexin Xu, and Ruikang K Wang. Influence of contact state on nir diffuse reflectance spectroscopy in vivo. *Journal of Physics D: Applied Physics*, 38(15):2691, 2005. URL `http://stacks.iop.org/0022-3727/38/i=15/a=022`.

Erina Cho, Richard Chen, Lukas-Karim Merhi, Zhen Xiao, Brittany Pousett, and Carlo Menon. Force myography to control robotic upper extremity prostheses: A feasibility study. *Frontiers in Bioengineering and Biotechnology*, 4:18, 2016. ISSN 2296-4185. doi: 10.3389/fbioe.2016.00018. URL `http://journal.frontiersin.org/article/10.3389/fbioe.2016.00018`.

H. S. Choi, H. D. Park, and K. J. Lee. Motion artifact reduction in blood pressure signals using adaptive digital filter with a capacitive sensor. In *2007 29th Annual International Conference of the IEEE Engineering in Medicine and Biology Society*, pages 3285–3287, Aug 2007. doi: 10.1109/IEMBS.2007.4353031.

Blaž Cugmas, Maksimilijan Bregar, Miran Bürmen, Franjo Pernuš, and Boštjan Likar. Impact of contact pressure–induced spectral changes on soft-tissue classification in diffuse reflectance spectroscopy: problems and solutions. *Journal of Biomedical Optics*, 19(3):037002, 2014. doi: 10.1117/1.JBO.19.3.037002.

C. J. De Luca, L. Donald Gilmore, M. Kuznetsov, and S. H. Roy. Filtering the surface emg signal: Movement artifact and baseline noise contamination. *Journal of Biomechanics*, 43(8):1573–1579, 2010. doi: 10.1016/j.jbiomech.2010.01.027.

DigikeyElectronics. Fsr400 short. `https://www.digikey.com/product-detail/en/interlink-electronics/34-00004/1027-1014-ND/2798665`.

Carlos Eduardo Ferrante do Amaral and Benhard Wolf. Current development in non-invasive glucose monitoring. *Medical Engineering And Physics*, 30(5):541 – 549, 2008. ISSN 1350-4533. doi: http://dx.doi.org/10.1016/j.medengphy.2007.06.003.

EeonTex. *NW170-SLPA-2k nonwoven pressure sensing fabric.*

HoneywellSensing. *FSA Series, Compensated/Amplified Force Sensor Data Sheet*, January 2017. Data sheet.

Inc. Interlink Electronics. *FSR Integration Guide.* Integration Guide.

Inc. Interlink Electronics. *FSR400 Series Data Sheet*, December 2013. Data sheet.

ISO 10993-1:2009(4). Biological evaluation of medical devices — part 1: Evaluation and testing within a risk management process. Standard, International Organization for Standardization, 2009.

M. Izzetoglu, A. Devaraj, S. Bunce, and B. Onaral. Motion artifact cancellation in nir spectroscopy using wiener filtering. *IEEE Transactions on Biomedical Engineering*, 52(5):934–938, May 2005. ISSN 0018-9294. doi: 10.1109/TBME.2005.845243.

T. Kiana and A. Michael. Wearable technology and wearable devices: Everything you need to know — wearabledevices.com. `http://www.wearabledevices.com/what-is-a-wearable-device`, March 2014. [Online; accessed 27-February-2017].

Reiner W. Kühl. Mechanical stress and deformation of smt components during temperature cycling and pcb bending. *Soldering & Surface Mount Technology*, 11(2):35–41, 1999. doi: 10.1108/09540919910265677.

Nan Li, Dapeng Yang, Li Jiang, Hong Liu, and Hegao Cai. Combined use of fsr sensor array and svm classifier for finger motion recognition based on pressure distribution map. *Journal of Bionic Engineering*, 9(1):39 – 47, 2012. ISSN 1672-6529. doi: http://dx.doi.org/10.1016/S1672-6529(11)60095-4.

Michael Meier-Schroers, Guido Kukuk, Rami Homsi, Dirk Skowasch, Hans Heinz Schild, and Daniel Thomas. MRI of the lung using the PROPELLER technique: Artifact reduction, better image quality and improved nodule detection. *European Journal of Radiology*, 85(4):707 – 713, 2016. ISSN 0720-048X. doi: https://doi.org/10.1016/j.ejrad.2015.12.016.

R. T. Nøstbakken. Feasibility of force sensing resistors as movement artifact detector in wearable devices. Project report, Norwegian University of Science and Technology, 2016.

O. A. Olsen. *Industrielle Målemetoder*. Jubok AS, 2^{nd} edition, 2015.

X. Pengjun, T. Xiaoming, and W. Shanyuan. Measurement of wearable electrode and skin mechanical interaction using displacement and pressure sensors. In *2011 4th International Conference on Biomedical Engineering and Informatics (BMEI)*, volume 2, pages 1131–1134, Oct 2011. doi: 10.1109/BMEI.2011.6098433.

Ltd. Pico Technology. *USB DrDAQ Data Logger User's Guide*, 2016. User Guide.

Ashkan Radmand, Erik Scheme, and Kevin Englehart. High-density force myography: A possible alternative for upper-limb prosthetic control. *Journal of Rehabilitation Research and Development*, 53(4):443 – 456, 2016. ISSN 07487711.

Nina Reistad, Mallory Mayjonade, Aylin Ahadi, and Stefan Andersson-Engels. Characterization of probe contact effects on diffuse reflectance spectroscopy measurements. volume 9531, pages 953143–953143–8, 2015. doi: 10.1117/12.2180917.

SSAL Seyedtabaii and L Seyedtabaii. Kalman filter based adaptive reduction of motion artifact from photoplethysmographic signal. *World Academy of Science, Engineering and Technology*, 37:173–176, 2008.

HanQun Shangguan, Scott A. Prahl, Steven L. Jacques, Lee W. Casperson, and Kenton W. Gregory. Pressure effects on soft tissues monitored by changes in tissue optical properties. volume 3254, pages 366–371, 1998. doi: 10.1117/12.308187.

Sparkfun. Pull-up resistors. `https://learn.sparkfun.com/tutorials/pull-up-resistors`, 2017. [Online; accessed 21-February-2017].

STMicroelectronics. *LM124, LM224, LM324 Low power quad operational amplifiers*, June 2011. Datasheet.

Inc. Tekscan. *FlexiForce Model A101*. Product page.

Inc. Tekscan. *FlexiForce Sensor Users Manual*, December 2010. User Manual.

TexasInstruments. *OPAx333 1.8-V, microPower, CMOS Operational Amplifiers, Zero-Drift Series*, March 2006. Datasheet, revised December 2015.

D. A. Tong, K. A. Bartels, and K. S. Honeyager. Adaptive reduction of motion artifact in the electrocardiogram. In *Proceedings of the Second Joint 24th Annual Conference and the Annual Fall Meeting of the Biomedical Engineering Society] [Engineering in Medicine and Biology*, volume 2, pages 1403–1404 vol.2, 2002. doi: 10.1109/IEMBS.2002.1106451.

Nienke van der Werf, Frans G.M. Kroese, Jan Rozing, and Jan-Luuk Hillebrands. Viral infections as potential triggers of type 1 diabetes. *Diabetes/Metabolism Research and Reviews*, 23(3):169–183, 2007. ISSN 1520-7560. doi: 10.1002/dmrr.695.

Fabrizio Vecchi, Cinzia Freschi, Silvestro Micera, Angelo M Sabatini, Paolo Dario, Rinaldo Sacchetti, et al. Experimental evaluation of two commercial force sensors for applications in biomechanics and motor control. In *5th Annual Conference of International Functional Electrical Stimulation Society*, 2000.

Tiesheng Wang, Meisam Farajollahi, Yeon Sik Choi, I-Ting Lin, Jean E. Marshall, Noel M. Thompson, Sohini Kar-Narayan, John D. W. Madden, and Stoyan K. Smoukov. Electroactive polymers for sensing. *Interface Focus*, 6(4), 2016. ISSN 2042-8898. doi: 10.1098/rsfs.2016.0026.

G. Wiechert, M. Triff, Z. Liu, Z. Yin, S. Zhao, Z. Zhong, R. Zhaou, and P. Lingras. Identifying users and activities with cognitive signal processing from a wearable headband. In *2016 IEEE 15th International Conference on Cognitive Informatics Cognitive Computing (ICCI*CC)*, pages 129–136, Aug 2016. doi: 10.1109/ICCI-CC.2016.7862025.

Wikipedia. Ip code. `https://en.wikipedia.org/w/index.php?title=IP_Code&oldid=780902550`, 2017a. [Online; accessed 01-June-2017].

Wikipedia. Apple watch. `https://en.wikipedia.org/w/index.php?title=Apple_Watch&oldid=767600481`, 2017b. [Online; accessed 27-February-2017].

Wikipedia. Refraction. `https://en.wikipedia.org/w/index.php?title=Refraction&oldid=775837217`, 2017c. [Online; accessed 25-April-2017].

Wikipedia. Samsung gear s3. `https://en.wikipedia.org/w/index.php?title=Samsung_Gear_S3&oldid=764287425`, 2017d. [Online; accessed 27-February-2017].

Wikipedia. Specular reflection. `https://en.wikipedia.org/w/index.php?title=Specular_reflection&oldid=772469508`, 2017e. [Online; accessed 25-April-2017].

Wikipedia. Wearable technology. https://en.wikipedia.org/wiki/Wearable_technology, 2017f. [Online; accessed 27-February-2017].

M. Wininger, N. H. Kim, and W. Craelius. Pressure signature of forearm as predictor of grip force. *J Rehabil Res Dev*, 45(6):883–92, 2008. ISSN 0748-7711.

L. B. Wood and H. H. Asada. Noise cancellation model validation for reduced motion artifact wearable ppg sensors using mems accelerometers. In *2006 International Conference of the IEEE Engineering in Medicine and Biology Society*, pages 3525–3528, Aug 2006. doi: 10.1109/IEMBS.2006.260359.

J. Yadav, A. Rani, V. Singh, and B. M. Murari. Near-infrared led based non-invasive blood glucose sensor. In *2014 International Conference on Signal Processing and Integrated Networks, SPIN 2014*, pages 591–594, 2014.

Chapter 6

Appendix

6.1 Importing Pspice models to TINA

To be able to simulate the transient response for operational amplifier from STMicroelectronics, the model needs to be added to the TINA software. The model was downloaded from STMicroelectronics.com, and is found under **HW Model, CAD Libraries & SVD**: LM324 Pspice model.

This is a .txt-file (*en.lm324.txt*) containing all the parameters for the OpAmp. The following steps were taken to install it:

1. File → Import → Pspice Netlist(*.CIR)
2. Close the file browser
3. In the Netlist editor → Copy over the details from en.lm324.txt downloaded from STMicroelectronics' website
4. Save it to directory of choice → a *.CIR is then created
5. Go to Tools → New Macro Wizard → Give it a name and browse for the newly created *.CIR-file
6. Click Next → Load shape from library → TEXAS → Be sure the pins in Netlist is assigned correctly to model's shape → Next
7. Save to directory of choice, or just use suggested → *.TSM-file is created

Step 6 can also be Autogenerated to a simple rectangle with numbers. Connect the right leads to the numbered pins according to en.lm324.txt-file:

1. Inverting input
2. Non-inverting input
3. Output
4. Positive power supply
5. Negative power supply

6.2 Supplementary plots

Troubleshooting

During early stages of the work presented in this thesis, a lot of noisy sessions were recorded with FSR and the use of DrDAQ. Significant signal steps of 54mV was seen quite regularly for tests measured using the Scope channel (see Figures 2.13 and 6.1b). It can also be seen in fig. 6.1a, where both Scope and EXT channel are connected to the output of the OpAmp, but supply voltage has been cut off. The EXT channel outputs 57mV (56.6mV with a multimeter) regardless of Scope connection, and this is interpreted as 54mV by the Scope. For Scope to give a higher value, EXT must be at least 108mV to trigger the next bit in the Scope ADC.

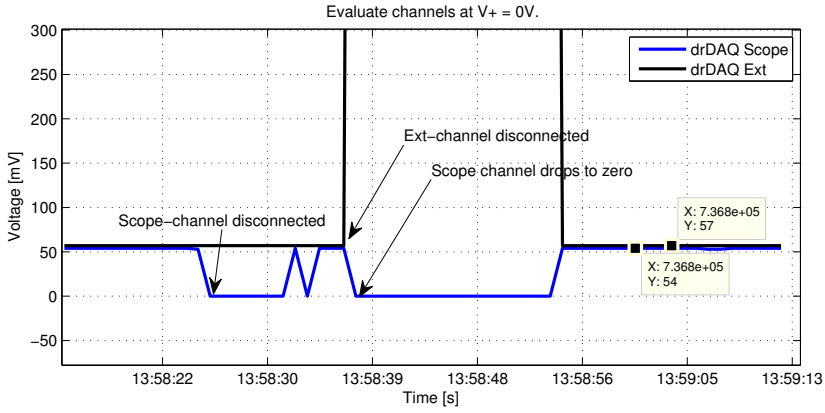

(a) Comparison of Scope and EXT channels with $V^+ = 0$

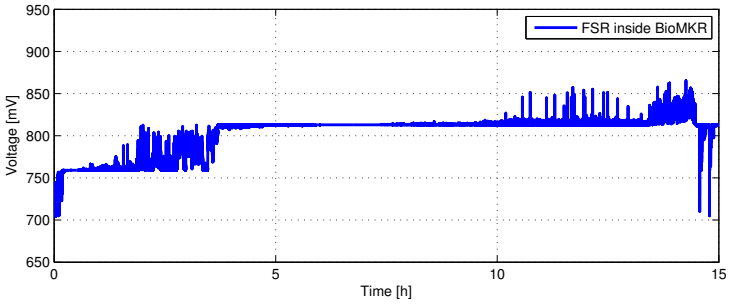

(b) 54mV signal jump

Figure 6.1: Noisy FSR signal during log sessions

Differences between test adapter and no adapter for strap testing

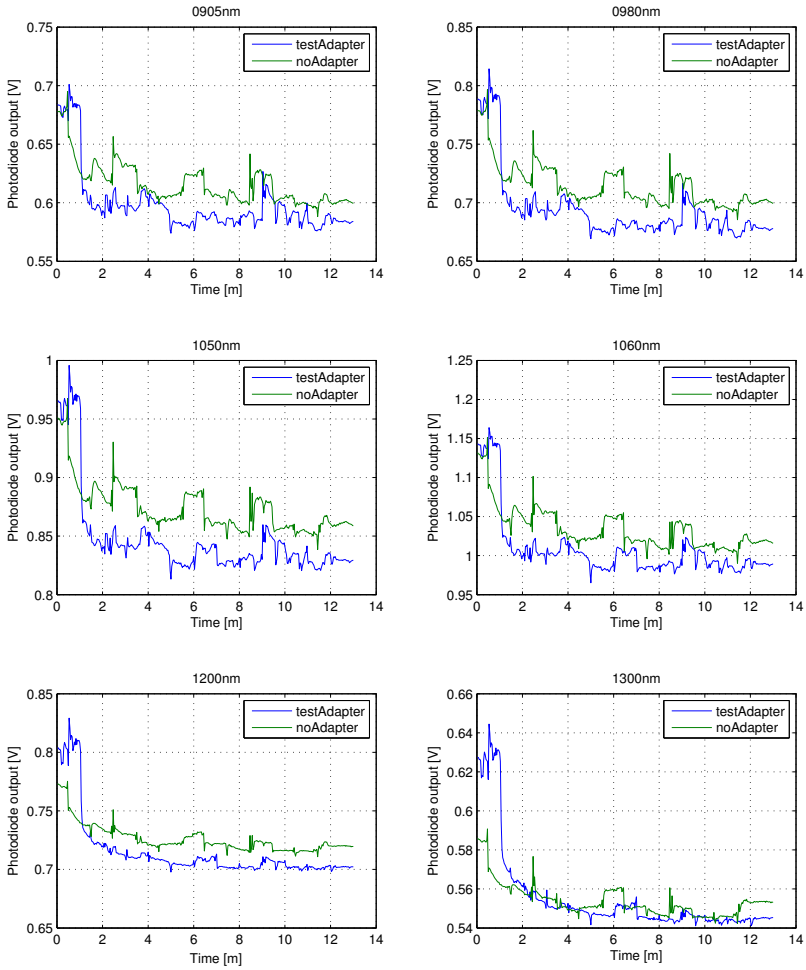

Figure 6.2: Strap test, comparison, 905-1300 nm

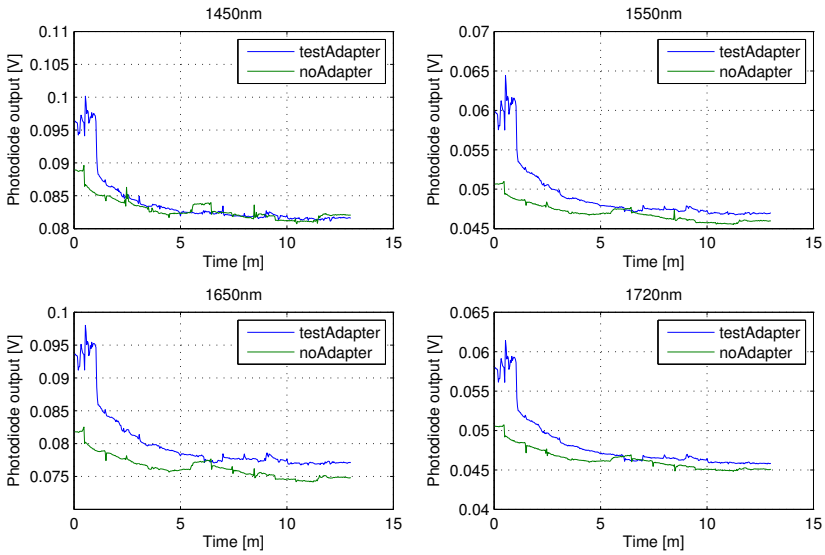

Figure 6.3: Strap test, comparison, 1450-1720 nm

NIR response during strap test for different adapters

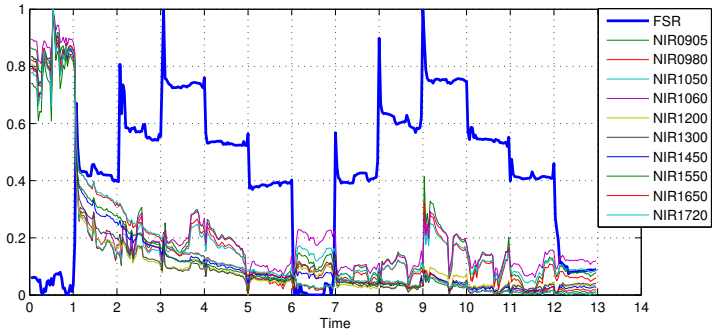

(a) Ø13T1.0TEST

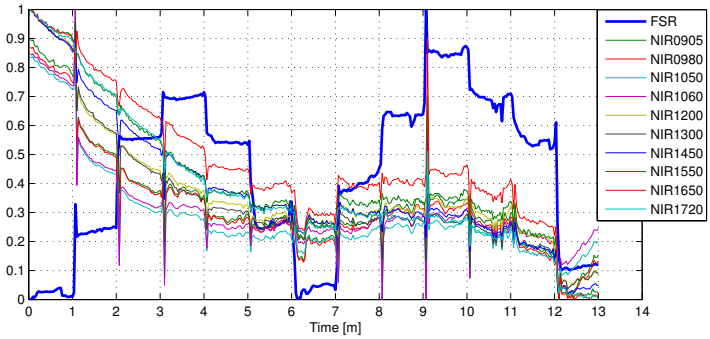

(b) Ø13T1.0FLAT

Figure 6.4: Strap tests, normalized

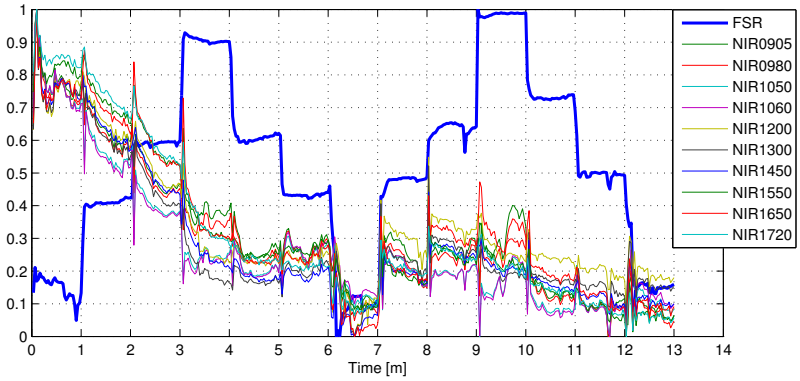

(a) Ø13T0.5CONE

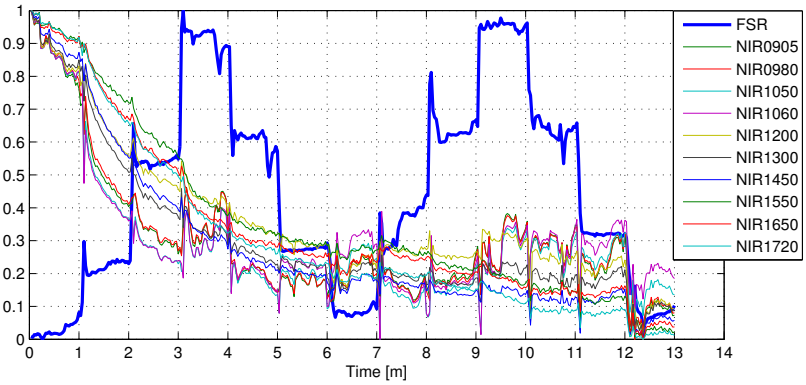

(b) Ø08T1.0FLAT

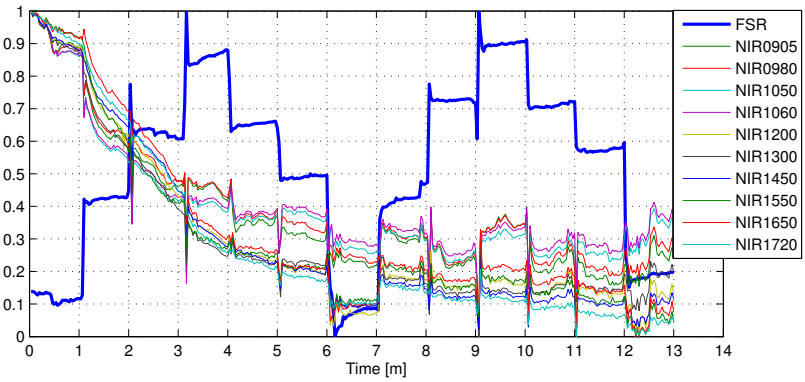

(c) Ø13T0.5FLAT

Figure 6.5: Strap tests, normalized

Segment	Mean	st.d	max	min
Loose-to-Loose	15.12	3.67	21.70 (NIR1550)	11.88 (NIR1060)
Loose-to-Light$_2$	15.50	2.74	20.81 (NIR1550)	12.59 (NIR1200)
Start-to-end	15.91	3.48	22.25 (NIR1550)	12.81 (NIR1200)

Table 6.1: Percent reduction in NIR signal value, Ø13T1.0TEST adapter

Segment	Mean	st.d	max	min
Loose-to-Loose	8.68	2.02	13.04 (NIR1720)	6.81 (NIR1200)
Loose-to-Light$_2$	8.59	1.72	12.21 (NIR1720)	6.12 (NIR1200)
Start-to-end	10.58	2.72	16.03 (NIR1720)	8.02 (NIR1200)

Table 6.2: Percent reduction in NIR signal value, Ø08T1.0FLAT adapter

Segment	Mean	st.d	max	min
Loose-to-Loose	9.39	1.76	13.57 (NIR1720)	7.53 (NIR1200)
Loose-to-Light$_2$	8.11	1.73	12.26 (NIR1720)	6.35 (NIR1200)
Start-to-end	9.46	2.27	14.69 (NIR1720)	7.38 (NIR1200)

Table 6.3: Percent reduction in NIR signal value, Ø13T0.5FLAT adapter

NIR response to external forces

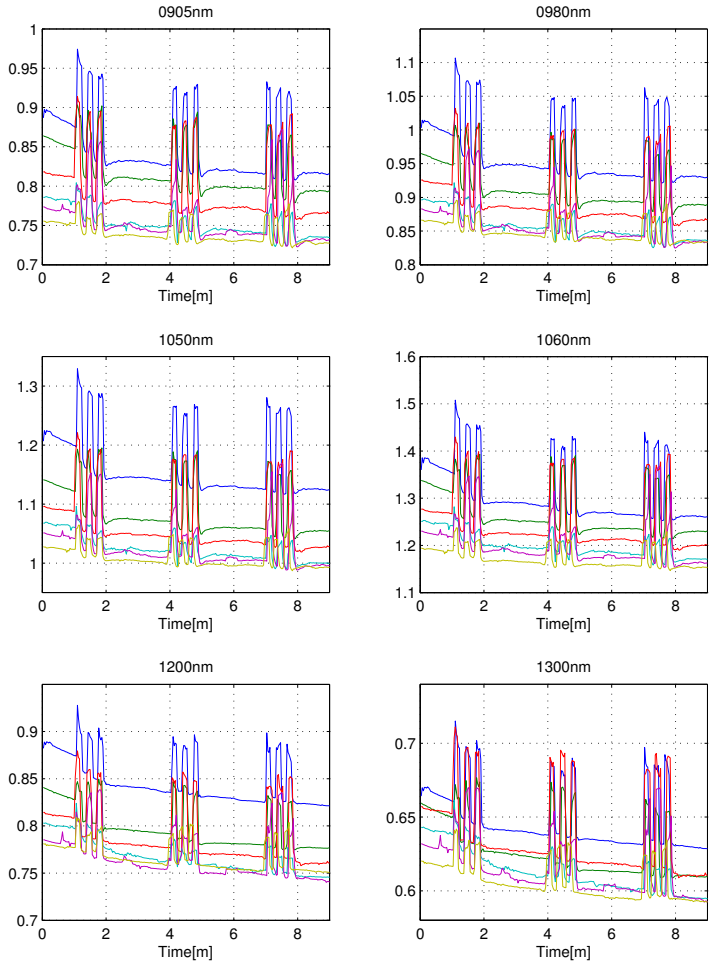

Figure 6.6: Response to external force, λ=905-1300nm

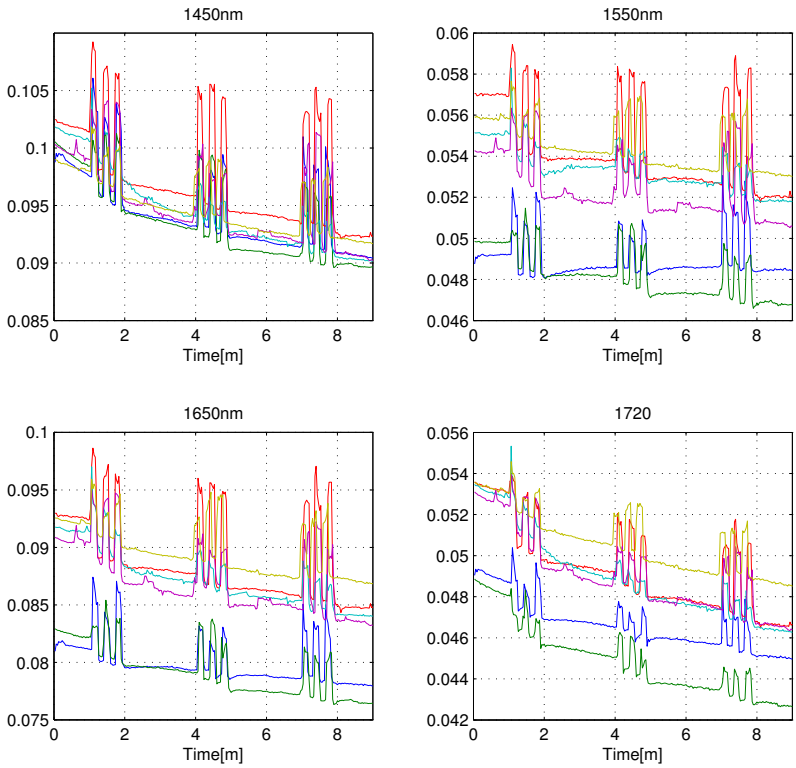

Figure 6.7: Response to external force, λ=1450-1720nm

	Mean (%)			
Wavelength	Segment 1-2	Segment 2-3	Segment 3-4	Segment 1-4, Total
NIR905	-3.02	-1.05	-1.12	-5.11
NIR980	-2.01	-0.81	-0.61	-3.39
NIR1050	-5.51	-1.33	-0.31	-7.0596
NIR1060	-5.01	-1.29	-0.49	-6.69
NIR1200	-3.91	-1.09	-0.99	-5.90
NIR1300	-3.97	-0.99	-1.19	-6.05
NIR1450	-2.97	-0.95	-0.96	-4.81
NIR1550	-1.88	-0.66	-0.52	-3.04
NIR1650	-5.78	-1.67	-0.44	-7.76
NIR1720	-5.34	-1.34	-0.48	-7.06

Table 6.4: Mean percent change in NIR values, Prototype II, L30W4T1.0FLAT

	Mean (%)			
Wavelength	Segment 1-2	Segment 2-3	Segment 3-4	Segment 1-4, Total
NIR905	-3.65	-1.03	-1.03	-5.62
NIR980	-4.02	-0.98	-1.15	-6.05
NIR1050	-3.09	-0.93	-1.02	-4.97
NIR1060	-1.91	-0.62	-0.51	-3.02
NIR1200	-4.70	-1.37	-0.71	-6.67
NIR1300	-4.63	-1.68	-0.55	-6.75
NIR1450	-3.85	-1.33	-1.12	-6.19
NIR1550	-4.10	-1.55	-1.20	-6.71
NIR1650	-3.10	-1.05	-1.01	-5.09
NIR1720	-1.94	-0.99	-0.47	-3.37

Table 6.5: Mean percent change in NIR values, Prototype II, Ø13T0.5CONE

	Mean (%)			
Wavelength	Segment 1-2	Segment 2-3	Segment 3-4	Segment 1-4, Total
NIR905	-3.76	-1.08	-0.59	-5.36
NIR980	-4.49	-1.75	-0.54	-6.67
NIR1050	-4.15	-1.43	-1.23	-6.69
NIR1060	-4.26	-1.64	-1.29	-7.05
NIR1200	-3.36	-1.16	-1.10	-5.54
NIR1300	-2.28	-1.15	-0.54	-3.93
NIR1450	-4.71	-2.12	-1.27	-7.92
NIR1550	-5.67	-2.87	-1.23	-9.50
NIR1650	-5.41	-2.33	-1.82	-9.31
NIR1720	-6.01	-3.03	-1.98	-10.67

Table 6.6: Mean percent change in NIR values, Prototype II, Ø13T1.0FLAT

	Mean (%)			
Wavelength	Segment 1-2	Segment 2-3	Segment 3-4	Segment 1-4, Total
NIR905	-5.18	-2.18	-1.86	-8.98
NIR980	-3.50	-2.12	-1.07	-6.55
NIR1050	-1.46	0.22	-0.22	-1.46
NIR1060	-3.23	-1.84	-1.02	-5.98
NIR1200	-5.53	-1.85	-1.53	-8.69
NIR1300	-2.99	-1.28	-1.74	-5.91
NIR1450	-4.33	-0.89	-1.45	-6.56
NIR1550	-2.76	-1.49	-0.72	-4.90
NIR1650	-2.30	-0.97	-0.88	-4.09
NIR1720	-3.59	-2.51	-1.13	-7.07

Table 6.7: Mean percent change in NIR values, Prototype II, Ø08T1.0FLAT

	Mean (%)			
Wavelength	Segment 1-2	Segment 2-3	Segment 3-4	Segment 1-4, Total
NIR905	-5.01	-2.09	-1.61	-8.49
NIR980	-4.43	-2.05	-1.79	-8.07
NIR1050	-4.67	-1.56	-1.76	-7.81
NIR1060	-2.99	-1.84	-0.88	-5.62
NIR1200	-4.55	-1.93	-1.71	-8.00
NIR1300	-6.18	-3.76	-2.04	-11.54
NIR1450	-7.17	-3.37	-2.39	-12.45
NIR1550	-7.04	-3.46	-2.60	-12.59
NIR1650	-7.09	-2.59	-2.36	-11.63
NIR1720	-4.48	-2.89	-1.52	-8.64

Table 6.8: Mean percent change in NIR values, Prototype II, Ø13T0.5FLAT

PLS regression

The numerical values producing Figure 4.3 are shown in Table 6.9, while the predicted FSR signal for various night tests using model built from two different night tests are shown in Figures 6.8 and 6.9.

	Regression coefficients				
Wavelength	Ø13T0.5 CONE	Ø13T0.5 FLAT	Ø13T1.0 FLAT	Ø08T1.0 FLAT	L30W4T1.0 RECT
NIR0905	18.86	22.36	-17.94	-24.63	0.13
NIR0980	-30.72	-33.99	2.10	-14.32	8.07
NIR1050	38.56	31.82	44.38	33.03	-17.25
NIR1060	-17.46	-19.11	22.72	-19.54	5.76
NIR1200	-7.25	-10.64	-6.85	28.38	-1.38
NIR1300	0.36	32.51	-5.03	-49.89	10.77
NIR1450	-37.28	-169.27	-54.98	111.89	4.00
NIR1550	-116.18	-126.24	-53.34	55.43	3.18
NIR1650	35.11	136.40	45.33	-22.76	6.16
NIR1720	197.72	81.91	185.44	-160.71	2.48

Table 6.9: Regression coefficients for the PLSR results form Table 4.1

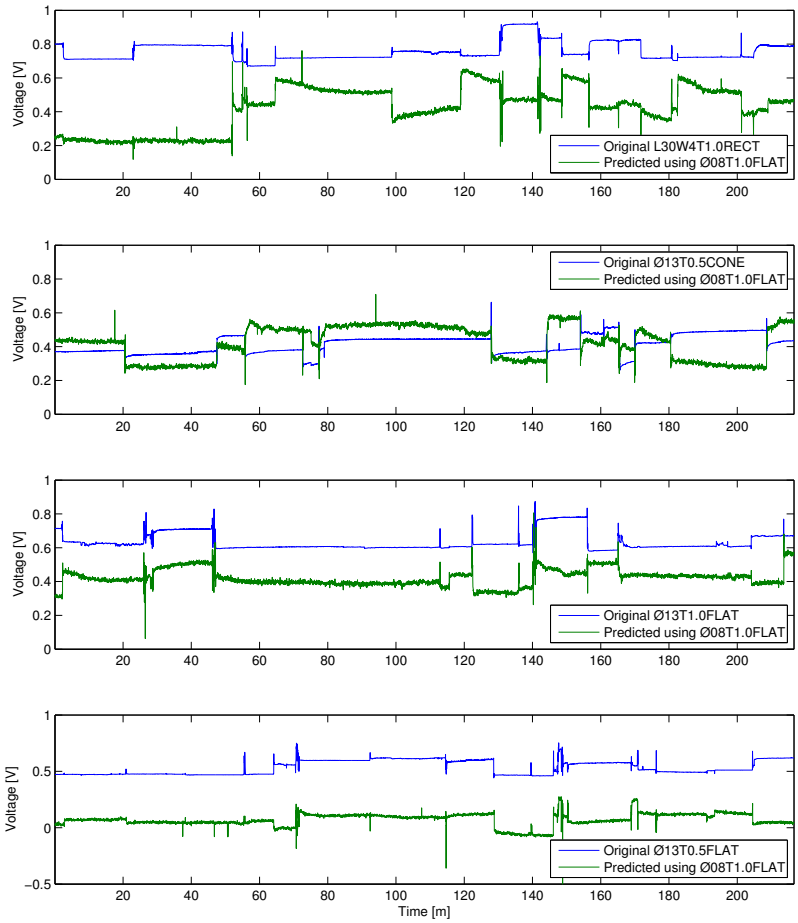

Figure 6.8: Attempt to recreate data set B with model from data set A, Ø08T1.0FLAT adapter

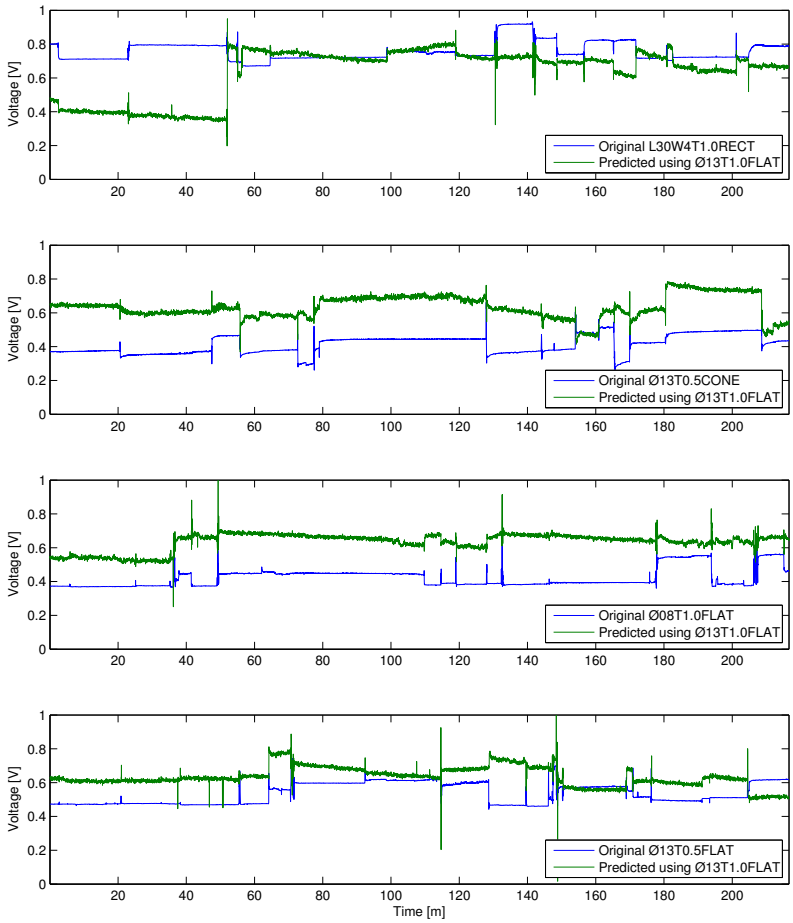

Figure 6.9: Attempt to recreate data set B with model from data set A, Ø13T1.0FLAT adapter